NTNU – Trondheim
Norwegian University of
Science and Technology

Scattering of Electromagnetic Waves from Randomly Rough Surfaces with Skewed Height Distributions

Erik Andreas Lydersen

Master of Science in Physics and Mathematics
Submission date: July 2014
Supervisor: Ingve Simonsen, IFY

Norwegian University of Science and Technology
Department of Physics

Abstract

Research on the scattering of electromagnetic waves from rough surfaces has greatly advanced in the past decades through the access to rigorous numerical simulations. However, most of the research has focused on surfaces with a Gaussian height distribution. In this thesis, the effect of the skewness of the surface height distribution on the scattering process is qualitatively examined. This is accomplished through rigorous numerical simulations of an electromagnetic field incident on rough surfaces with different values for the surface height skewness. Both the reflection from opaque materials and transmission from transparent materials are studied. For the reflected field, strongly skewed surface heights were found to induce more scattered intensity in the forward direction, both for positive and negative values of the skewness. For negative values, there was an additional increase in the scattered intensity for large angles in the forward direction. A negative correlation was found between the surface height skewness and the size of the enhanced backscattering peak. For non-normal angles of incidence, the intensity in large angle backward directions was found to have a negative correlation with the surface height skewness. For absorbing materials, the absorption rate did not seem to be affected by the surface height skewness. The coherent component of the scattered field from weakly rough surfaces appeared to be slightly larger both for large positive and large negative values of the surface height skewness. For the transmitted field from transparent materials, the effects of positive and negative values of the surface height skewness were the same, and only the magnitude had an effect. For a normal angle of incidence, larger magnitudes of the surface height skewness induced less diffusion, while for oblique angles of incidence the effect was opposite. The transmittance seemed to be independent of the surface height skewness. Plausible explanations of the effects are given by modelling a surface with strongly skewed surface heights as a relatively flat surface with a few of tall peaks or deep pits.

Sammendrag

Forskning på spredning av elektromagnetiske felt fra tilfeldig ru overflater har utviklet seg svært mye gjennom tilgang til numeriske simuleringer. Det meste arbeidet har vært fokusert på overflater med en gaussisk høydefordeling. I denne avhandlingen blir spredning fra overflater med en skjev gaussisk fordeling kvalitativt undersøkt. Dette gjøres gjennom rigorøse numeriske simuleringer av en elektromagnetisk stråle rettet mot overflater med forskjellig grad av skjevhet i høydefordelingen. Både refleksjon fra ugjennomsiktige materialer og transmisjon fra gjennomsiktige materialer blir undersøkt. For refleksjon fra ugjennomsiktige materialer viste resultatene en økning i intensiteten i fremoverretningene for økende skjevhet i høydefordelingen, både for positive og negative verdier av skjevheten. For negative verdier var det en ekstra økning for store vinkler i fremoverretningen. En negativ korrelasjon ble funnet mellom skjevheten i høydefordelingen og størrelsen på toppen forårsaket av forsterket tilbakespredning. For ikke-normalt innfall hadde spredningen ved store vinkler i bakoverretningen en negativ korrelasjon med skjevheten i høydefordelingen. Absorpsjonskoeffisienten for absorberende materialer viste ingen tydelig korrelasjon med skjevheten i høydefordelingen. Den koherente komponenten for svakt ru overflater var noe større for både store positive og store negative verdier av skjevheten i høydefordelingen. For det transmitterte feltet fra gjennomsiktige materialer hadde fortegnet til skjevheten i høydefordelingen neglisjerbar betydning, og bare størrelsen absoluttverdi hadde noe å si. For vinkeltrett innfall førte lavere absoluttverdi til mindre diffusjon, mens for skrått innfall var effekten motsatt. Transmittansen viste ingen avhengighet av skjevheten i høydefordelingen. Mulige forklaringer på alle disse effektene blir gitt ved å modellere en overflate med stor skjevhet i høydefordelingen som en relativt flat overflate med noen få skarpe topper eller bunner.

Contents

Preface

This thesis was written as a completion of my Master's degree of Physics and Mathematics with specialization in Applied Physics at the Norwegian University of Science and Technology.

My sincere gratitude goes to my supervisor Ingve Simonsen, without whom this thesis would not have been possible. Not only because it was his simulation program that was used to produce the results, but mainly because he always found the time to help as much as needed. He has been infinitely patient in helping me with my clever bugs, and I am extremely grateful for his never-ending insistence that I double-check everything one more time. The motto "Skynd deg sakte" ("Hurry, but slowly") is one that I will try to apply as I begin my life outside of studies.

Also thanks to Terje Røsten at the Institute of Physics for help with access to the computer cluster as well as software installation.

Lastly, a big thanks to Arja Sue-Chu, Solveig Berthung and Morten Hatlen for proof-reading and feedback.

List of Figures

Chapter 1

Introduction

Maxwell's equations were formalized in the late 1800s and form the foundation of electrodynamics and optics. From these equations one can derive the Fresnel equations, which are used to calculate how electromagnetic waves reflect and transmit when encountering an interface between two media with different refractive indices. A basic assumption for the Fresnel equations is that the interface is flat, but no real surface is perfectly flat on every scale. No matter how smooth a surface may seem, it is bound to be rough on a microscopic scale as all matter is made out of (non-flat) atoms. In other words, the roughness of a surface is relative and dependent on the probe used to observe it. If the surface is sufficiently rough, the Fresnel equations no longer apply and other methods must be used to investigate the scattering of electromagnetic waves. Such methods have been developed both for numerical simulations and experiments, and an excellent review paper describing the concepts of the topic is found in Ref. [1]. The interested reader is referred to this review for a full theoretical basis of rough surface scattering, while only the concepts relevant to this thesis will be explained here.

With regards to numerical simulations, most previous work is done on surfaces where the height of the surface is normally distributed. This is largely due to practical reasons: the normal distribution is well studied and understood, the moments of any order can be related to the first two and surfaces with this height distribution are relatively easy to generate numerically. In addition, such surfaces can be made experimentally, allowing experimental verification of numerical simulations.

While these are good reasons to work with the normal distribution, many surfaces, if not most, do not have normally distributed heights. Examples of this relevant to this work are surfaces treated with acid or processes similar to abrasive blasting, where a high pressure stream of particles removes material

from the surface. A common feature of acid treated surfaces is pits where the acid gathers due to gravity and creates deep and narrow structures, while the surrounding area remains relatively unaffected due to shorter exposure times. Abrasive blasting, on the other hand, can leave sharp peaks at locations where the material is harder than elsewhere, for instance due to impurities or structural anomalies. Both these processes leave the surfaces with an asymmetric height distribution with respect to the surface mean. Hence, such surfaces are poorly approximated by a symmetric normal height distribution.

The purpose of this thesis is to explore how the skewness of the surface height distribution affects the scattering process. This will be accomplished by creating rough surfaces with a height distribution which has a tunable skewness, and running rigorous numerical simulations for different values of this skewness.

1.1 Thesis structure

The work in this thesis is divided into three parts, and the relevant theory will be explained in each Chapter. All uncited Figures were created by the author.

Chapter 2 gives a more formal description of rough surfaces and how they are represented numerically.

Chapter 3 describes a random number generator for a skewed distribution. The choice of the skew normal distribution as a height distribution is motivated and the relevant properties of the distribution are given. Further, the method of random number generation is explained before the results of the implementation of the random number generator are presented. This Chapter is a modified version of a project report which was written as a preparation for this thesis [2].

Chapter 4 presents an algorithm for generating properly correlated surfaces from uncorrelated random numbers. A modification of this algorithm is motivated and explained, before the results of its implementation are presented.

Chapter 5 explains the basics of rough surface scattering simulations as well as some metrics used to verify the validity of the results. Some adjustments of the surfaces were necessary to give realistic results, and these methods are explained and their impact on the surface statistics are shown.

Chapter 6 shows the results of rigorous numerical simulations of scattering from surfaces with various skewness, and the impact of this skewness on the scattering process is discussed.

Chapter 7 summarizes and concludes the methods and results presented in this thesis.

Chapter 8 suggests further work and topics of research relevant to the presented material.

Chapter 2

Theory of rough surfaces

In this Chapter the characteristics of rough surfaces are described and the tools necessary to represent such surfaces numerically are outlined.

2.1 A 'rough' guide

A qualitative comparison between rough and smooth surfaces is shown in Fig. 2.1. The surface may be considered smooth if all or most the incident light is scattered in the specular direction, as shown in Figs. 2.1a-b. If the surface becomes sufficiently rough, most of the light is scattered in other directions, as shown in Figs. 2.1c-d. This is called diffuse or incoherent scattering.

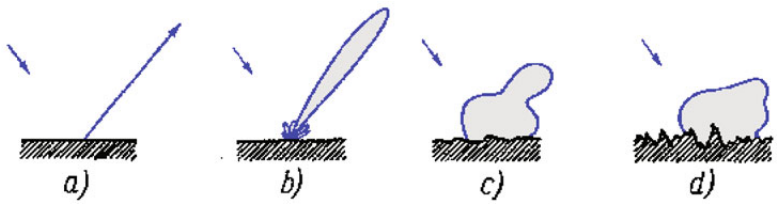

Figure 2.1: Illustration of the transition between rough and smooth scattering. Figure 2.1a shows a smooth surface, and all the incident light, indicated by the arrow, is scattered in the specular direction. Moving right towards Fig. 2.1d, the surfaces become more rough, resulting in less specular and more diffuse scattering [1, Fig. 1].

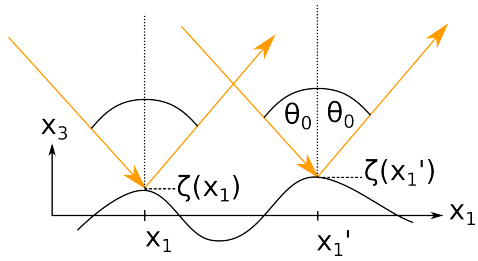

Figure 2.2: Basic geometry of specular scattering from a rough surface.

The concept of roughness can be made quantifiable by examining a surface $x_3 = \zeta(x_1)$ oriented so that x_1 is along the surface mean. If two coherent rays of light are scattered from two arbitrary points $(x_1, \zeta(x_1))$ and $(x_1', \zeta(x_1'))$ on the surface, a phase difference $\Delta\phi$ arises in the outgoing rays. If the angle between the incoming rays and x_3 is θ_0, the specular component by definition forms an angle θ_0 with the x_3 axis (Snell's law of reflection). An illustration of the geometry is shown in Fig. 2.2. In isotropic media the phase difference is equal to the difference in path length multiplied by the wave number. In this simple geometry the phase difference of the outgoing waves is

$$\Delta\phi = 2|\mathbf{k}||\zeta(x_1) - \zeta(x_1')|\cos(\theta_0), \tag{2.1}$$

where $|\mathbf{k}| = 2\pi/\lambda$ is the modulus of the incoming wave vector[1, Eq. 1]. If $\zeta(x_1) = \zeta(x_1')$ for all x_1, the surface is perfectly flat and the phase difference $\Delta\phi$ is always zero. If $\Delta\phi \ll \pi$ the outgoing rays still interfere constructively, and the surface may still be considered smooth, as shown in Fig. 2.1b. However, if $\Delta\phi \simeq \pi$ the waves interfere destructively and the scattered intensity in the non-specular directions are comparatively larger. This corresponds to a rough surface as shown in Fig. 2.1d. Thus, $\Delta\phi = \pi/2$ may be considered a borderline between rough and smooth: The surface is smooth if $\Delta\phi < \pi/2$, otherwise it is rough. This is called the Rayleigh criterion after the physicist Lord Rayleigh.

The height difference between two arbitrary points on the surface is not a very consistent way of measuring surface roughness. This height difference is instead replaced with the root-mean-square (RMS) height or standard deviation δ of the height fluctuations from the surface mean. This makes the Rayleigh criterion for rough surfaces [1, Eq. 2]

$$|\mathbf{k}|\delta\cos(\theta_0) < \frac{\pi}{4}. \tag{2.2}$$

The parameters of the probe, $|\mathbf{k}|$ and θ_0, determine whether a physical surface characterized by δ should be considered rough or smooth. If the wavelength is

large compared to the height fluctuations, the product $|\mathbf{k}|\delta$ becomes small and the surface is smooth. The same surface may be considered rough if the wavelength of the probe is comparable to or smaller than δ. Similarly, a rough surface may become smooth if the angle θ_0 grows large enough, even though the wavelength of the incoming waves and the physical surface are the same.

2.2 Representing rough surfaces

Continuous surfaces must be discretized to be represented numerically. The surface is thus sampled at N discrete points separated by a sampling interval Δx_1. This gives a set of points $\xi_n = n\Delta x_1$, with $n = 0, 1, 2, \ldots, N-1$. The sampling interval should be chosen in accordance with the Nyquist criterion for maximum resolvable frequency [3]. In the context of rough surface scattering, it must be chosen such that both the wavelength λ of the incident light and the correlation length a of the surface are well resolved. This correlation length is a characteristic parameter of a rough surface, which will reappear shortly in the context of autocorrelation functions. Next, the notation for discrete surfaces used in Appendix A of Ref. [4] is introduced, where

$$\zeta(\xi_n) = \delta \sum_{j=-\infty}^{\infty} W_j X_{j+n} \tag{2.3}$$

is the surface height at ξ_n. Here, δ is the standard deviation or RMS roughness of the surface, $\{X_n\}$ is a set of random, uncorrelated numbers and $\{W_j\}$ is a set of weights. Note that this implies a limitation on the surface profiles: only one value of ζ is possible for each ξ_n, hence surfaces with overhangs are not possible to represent with this notation. The two sets $\{X_n\}$ and $\{W_j\}$ determine the statistical properties of the surface, and their requirements and impact on these statistics will now be explained.

The random numbers $\{X_n\}$ determine the height distribution of the surface, hence the set of heights $\{\zeta(\xi_n)\}$ will have the same overall statistics as $\{X_n\}$ regardless of the weights $\{W_j\}$. To ensure that the surface is oriented along the x_1 axis, a vanishing average is required, as

$$\langle X_n \rangle = 0 \Rightarrow \langle \zeta(\xi_n) \rangle = 0. \tag{2.4}$$

The angle brackets denote an average over an ensemble of surface realizations. Furthermore, if the RMS roughness of the surface is to be determined by δ, the random numbers $\{X_n\}$ must have a standard deviation of 1.

The weights $\{W_j\}$ determine the height-height correlation (autocorrelation) of the surface, and these weights should be chosen in such a way that the surface

has the desired correlation function $W(|x_1|)$. For the surface heights $\zeta(\xi_n)$, this correlation property is expressed by

$$\langle \zeta(\xi_k)\zeta(\xi_{k+l})\rangle = \delta^2 W(|\xi_k - \xi_{k+l}|). \tag{2.5}$$

To ensure that δ alone determines the RMS roughness of the resulting surface, the correlation function needs to be normalized, i.e. $W(0) = 1$. The effect of different correlation functions on rough surface scattering has been examined previously and is not the focus of this work. Hence, the Gaussian correlation function will be used consistently here. The properly normalized form is given by [1, Eq. 8a]

$$W(|x_1|) = \exp\left(-\frac{x_1^2}{a^2}\right). \tag{2.6}$$

Here a is the previously mentioned correlation length of the surface. This length is effectively a transversal scale parameter along the x_1 axis, and it is of paramount importance to choose a sampling interval Δx_1 which is significantly smaller than a.

Another quantity needed for generating surfaces is the power spectral density (PSD) function. According to the Wiener-Khinchin theorem [5], the autocorrelation function and the PSD function are related via a Fourier transform. (This assumes a stationary process and that the Fourier transform of the autocorrelation function exists. This is a stationary process due to ensemble averaging.) The PSD function in the case of Gaussian autocorrelation is given by [1, Eq. 8b]

$$g(k) = \sqrt{\pi} a \exp\left(-\frac{a^2 k^2}{4}\right). \tag{2.7}$$

The surfaces used in this work are defined only by the height distribution and (first order) autocorrelation function. These are the most common quantities used to describe random correlated signals, and other quantities such as higher order correlations will be assumed negligible.

The next Chapter describes a random number generator which is used to generate $\{X_n\}$, while Chapter 3 shows how the weights $\{W_j\}$ are manipulated to give a surface generation algorithm.

Chapter 3

A skewed random number generator

A skew normal distribution as described by A. Azzalini was chosen for the random numbers X_n [6], and the details on its properties are presented in the next Section. This distribution has a skewness parameter which can be used to tweak the skewness within a certain range, and setting this parameter to zero gives the normal distribution. This property is very useful as it allows a gradual transition from the previously studied case of the normal distribution to a skewed distribution. Comparing simulation results with different skewnesses will show which, if any, scattering effects are stronger or weaker for a surface with a skewed height distribution. A description of the distribution is given along with the method of number generation, before the results of the generated numbers are presented.

3.1 Properties of the skew normal distribution

The skew normal distribution has the form

$$f(x) = \frac{2}{\omega}\phi\left(\frac{x-\xi}{\omega}\right)\Phi\left(\alpha\left(\frac{x-\xi}{\omega}\right)\right). \tag{3.1}$$

Here, $\phi(x)$ is the standard normal probability density function given by

$$\phi(x) = \frac{1}{\sqrt{2\pi}}\exp(-\frac{x^2}{2}) \tag{3.2}$$

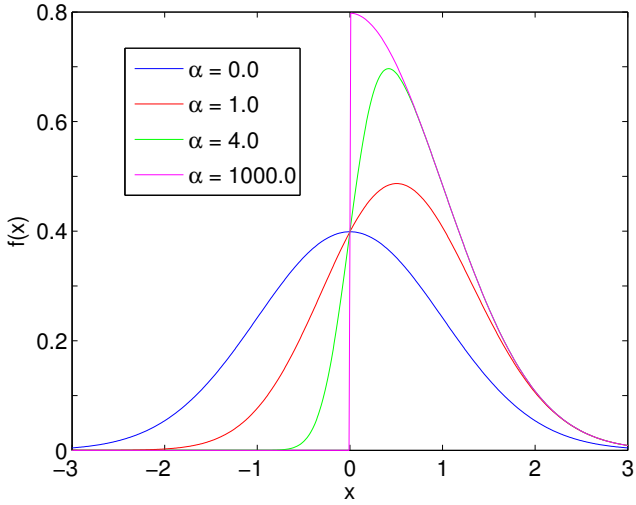

Figure 3.1: $f(x)$ plotted for several values of α with $\xi = 0$ and $\omega = 1$.

and $\Phi(x)$ is the cumulative distribution function of the normal distribution given by

$$\Phi(x) = \int_{-\infty}^{x} \phi(x')\,\mathrm{d}x'. \tag{3.3}$$

The parameters α, ξ and ω are shape, location and scale, respectively. The parameter α defines the skewness of the distribution, and examples of $f(x)$ with different values of α are shown in Fig. 3.1. If $\alpha = 0$, then $\Phi(0) = \frac{1}{2}$ and $f(x)$ is equal to the normal distribution. In this special case ξ is the mean and ω is the standard deviation. Note that this is not true for any $\alpha \neq 0$. The distribution is right skewed for $\alpha > 0$ and left skewed for $\alpha < 0$. It is also antisymmetric about α: the distribution is mirrored about ξ as $\alpha \to -\alpha$. As α grows large, the distribution tends towards two times the half normal density as shown in Fig. 3.1 when $\alpha = 1000$.

The first three moments of the distribution are needed to ensure a zero mean and a variance of 1, and to know the relation between α and the skewness of the distribution. They can be found by calculating the moment-generating function, given for a stochastic variable X with a probability density function $p(x)$ by

$$M_X(t) = \mathrm{E}(\mathrm{e}^{tX}) = \int_{-\infty}^{\infty} p(x)\mathrm{e}^{tx}\,\mathrm{d}x. \tag{3.4}$$

The nth moment is then given by

$$\mathrm{E}(X^n) = \left.\frac{\partial^n M_X}{\partial t^n}\right|_{t=0}. \tag{3.5}$$

The moment-generating function of a skew normal variable Z with $\xi = 0$ and $\omega = 1$ is given in Ref. [6] as

$$M_Z(t) = 2\exp(t^2/2)\Phi(\delta t) \tag{3.6}$$

with $\delta = \alpha/\sqrt{1+\alpha^2}$. For a skew normal variable X with location ξ and scale ω, the moment-generating function is

$$M_X(t) = M_{\omega Z+\xi}(t) = \exp(\xi t)M_Z(\omega t) = 2\exp\left(\frac{\xi t + (\omega t)^2}{2}\right)\Phi(\delta\omega t). \tag{3.7}$$

Applying Eq. (3.5) to Eq. (3.7) gives the first three moments

$$\mu \equiv \mathrm{E}(X) = \xi + \omega\delta\sqrt{\frac{2}{\pi}}, \tag{3.8}$$

$$\sigma^2 \equiv \mathrm{E}(X^2) = \omega^2\left(1 - \frac{2\delta^2}{\pi}\right) \tag{3.9}$$

and

$$\gamma \equiv \mathrm{E}(X^3) = \frac{4-\pi}{2}\frac{\left(\delta\sqrt{2/\pi}\right)^3}{(1-2\delta^2/\pi)^{3/2}}. \tag{3.10}$$

The symbols μ, σ and γ will be used for mean, standard deviation and skewness, respectively. The skewness of the distribution cannot grow without bounds, but is limited to the interval $(-\gamma_{max}, \gamma_{max})$ where $\gamma_{max} \approx 0.995$. This can be shown by first noting that δ is a monotonically increasing function of α and is limited to the interval $(-1, 1)$. It is not immediately apparent that γ is monotonically increasing, but this is shown with a quick calculation. The monotonic properties of γ are the same as those of $h(\delta) = \delta^3/(1-\frac{2\delta^2}{\pi})^{3/2}$, and the derivative of $h(\delta)$ is

$$\begin{aligned}\frac{\mathrm{d}}{\mathrm{d}\delta}h(\delta) =& \frac{3\delta^2(1-2\delta^2/\pi)^{3/2} - \delta^3\cdot\frac{3}{2}(1-2\delta^2/\pi)^{1/2}(-\frac{4\delta}{\pi})}{(1-2\delta^2/\pi)^3} \\ =& \frac{3\delta^2}{(1-2\delta^2/\pi)^{5/2}}.\end{aligned}$$

This expression is non-negative and real for $\delta^2 < \frac{\pi}{2}$, and thus $\gamma(\delta)$ is also monotonically increasing on the interval $-\frac{\pi}{2} < \delta < \frac{\pi}{2}$. As $\delta(\alpha)$ is limited to $(-1, 1)$, γ is monotonically increasing for all α and the limits $\delta = \pm 1$ give the corresponding limits on γ. The maximally skewed distribution is shown in Fig. 3.1 when $\alpha = 1000$. The skewness γ as a function of the shape parameter α is shown as a solid line in the upper graph of Fig. 3.6 on page 14.

3.2 A method for generating skew normal random numbers

For the application at hand, the properties $\mu = 0$ and $\sigma = 1$ are desired, as scaling will be done later. This is accomplished by choosing $\omega = 1/(1 - 2\delta^2/\pi)$ and $\xi = -\omega\delta\sqrt{2/\pi}$ for the chosen α. Then, the rejection method as described in Subsection 7.3.6 of Ref. [7] is used, which will be briefly described here.

Suppose that a random number generator for the probability distribution $p(x)$ is desired. If it was possible to generate uniformly distributed points in two dimensions under the graph of $p(x)$, the x-values of those points would have the desired distribution. Suppose further that there exists a function $g(x) \geq p(x)$ for all x for which a random number generation algorithm is known (e.g. normal distribution, uniform distribution...). To generate a set of points uniformly distributed under the graph of $g(x)$, a set $\{x_i\}$ of random numbers from $g(x)$ is first generated. For each x_i a second random number y_i is generated from a uniform distribution on the interval $[0, g(x_i)]$. The set $\{x_i, y_i\}$ is now uniformly distributed under $g(x)$. Hence, the subset that lie under the graph of $p(x)$ are also uniformly distributed. By rejecting the points with $y_i > p(x_i)$, the remaining $\{x_i\}$ have the desired distribution. This gives the following algorithm, illustrated in Fig. 3.2:

1. Find a function $g(x) \geq p(x)$ for all x with a known method of random number generation.
2. Generate a random number x_0 from $g(x)$.
3. Generate a random number y_0 from a uniform distribution on the interval $[0, g(x_0)]$.
4. Accept x_0 if $y_0 \leq p(x_0)$, otherwise reject it and go back to step 2.

In the case of the skew normal distribution $f(x)$, $\Phi(x) < 1$ for all x (it is the cumulative of the normal distribution, so $\lim_{x\to\infty} \Phi(x) = 1$) and thus

$$f(x) < \frac{2}{\omega}\phi(\frac{x-\xi}{\omega}) \equiv g(x). \tag{3.11}$$

The right hand side of Eq. (3.11) is the normal distribution scaled by a factor of two. Normal deviates are easily generated using for instance the Marsaglia polar method [8]. A note on the rejection method's effectiveness is that it depends on the choice of $g(x)$. In this case the area under the curve of $g(x)$ is twice as large as the area under the curve of $f(x)$. This implies that it takes on average two random normal numbers to generate one random skew normal number. The method and results presented in this section were used to implement a random number generator for skew normal numbers in the Fortran 90 programming language.

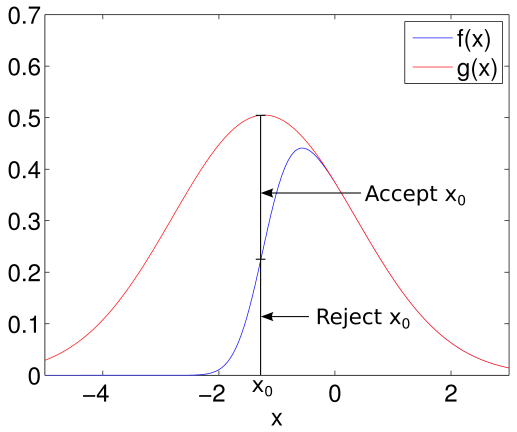

Figure 3.2: Illustration of the rejection method. Here, $p(x) = f(x)$ with $\alpha = 4$ and $g(x)$ is a normal distribution multiplied by 2.

3.3 Results and discussion

To test the generator, samples of $N = 2 \cdot 10^7$ numbers were generated with varying α and the mean, variance and skewness were compared to the expected values. The results are shown in Figs. 3.3-3.6. Figure 3.3 shows a histogram of the sample with $\alpha = -8$ along with the corresponding probability density function, demonstrating that the numbers are from a skew normal distribution. Due to the central limit theorem the mean, variance and skewness of the samples have a normal distribution with expected values 0, 1 and $\gamma(\alpha)$, respectively. The standard deviation for the mean of each sample is $1/\sqrt{N} \simeq 2.2 \cdot 10^{-4}$, and this is consistent with the size of the fluctuations shown in Fig. 3.4. Determining the standard deviation of the second and third moments requires some calculation, and is shown in Appendix A. The standard deviation of the second moment has an α dependence and is shown in Fig. 3.5. The analytical standard deviation is around $3 \cdot 10^{-4}$ near $\alpha = 0$ and converges towards approximately twice the size as $|\alpha|$ grows. The fluctuations in the second moment are somewhat smaller than expected, as 20 of 21 samples lie within one standard deviation. (For a normal distribution about 70% of the samples are expected to be found within one standard deviation, which in this case is around 14-15.) The upper graph of Fig. 3.6 shows γ as a function of α along with the mean value of the skewness for the generated samples. The lower graph shows the deviations from the expected values, indicating fluctuations of the size 10^{-3}. Again, 20 of 21 samples lie within

one standard deviation, so the fluctuations are smaller than expected.

During the early testing of the generator, the observed variance and skewness of the samples were consistently smaller than the expectation by a few percent, and never larger, as would normally be the case in about half the samples. This turned out to be a problem with the numeric precision. Taking the variance as an example, this is on average in the order of magnitude of 1. As the sample grows large, the relative contribution of each generated number to the total variance is of the order of magnitude $1/N \simeq 10^{-7}$. This gave a rounding error in the total variance as many of the contributions were too small and neglected, but this was easily fixed by adjusting the generator from single to double precision.

The same rounding error was suspected to be the cause of the smaller-than-expected fluctuations in the second and third moment, but reducing the sample size N to as little as 10^4 did not change the outcome. In the end this discrepancy was assumed to be a numerical artefact, and was not investigated further as the number generator produces random numbers with an accuracy well within the requirements of this application.

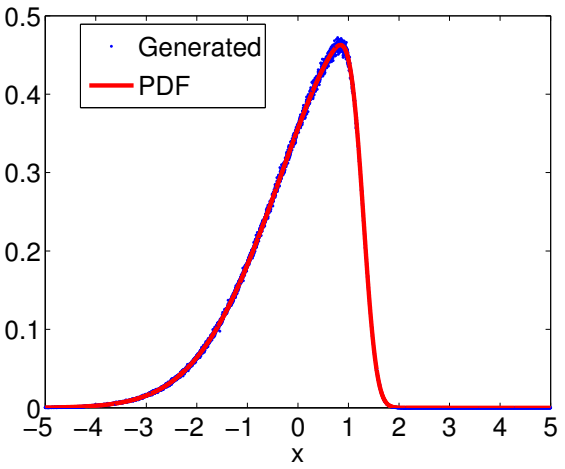

Figure 3.3: A scaled histogram of a sample of $N = 2 \cdot 10^7$ generated numbers with $\alpha = -8$ with the corresponding analytical probability density function (PDF) for comparison.

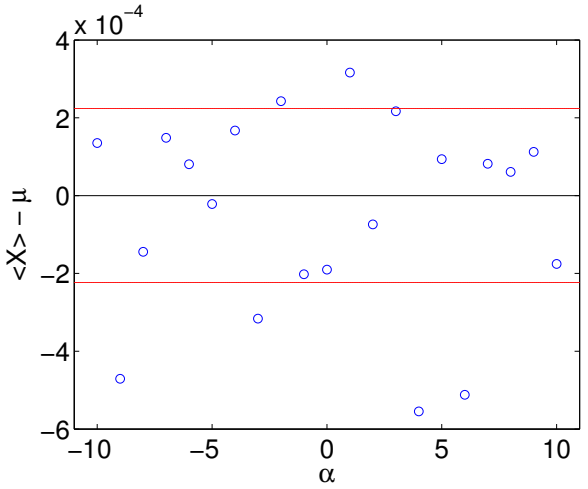

Figure 3.4: Sample deviations from the expected $\mu = 0$ for different values of α. The sample size was $N = 2 \cdot 10^7$ and the red lines indicate one standard deviation.

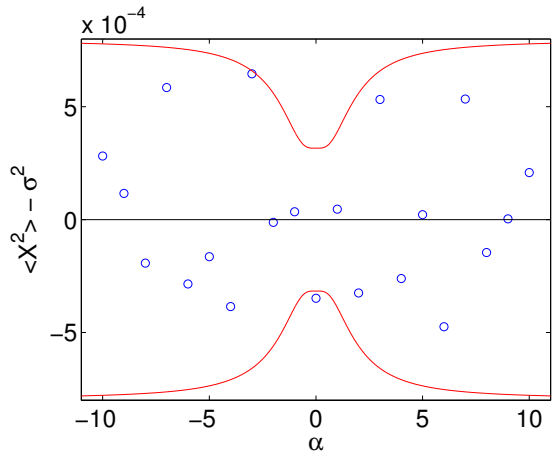

Figure 3.5: Sample deviations from the expected variance $\sigma = 1$ for the same samples as those shown in Fig. 3.4. The red lines indicate one standard deviation as calculated in Appendix A.

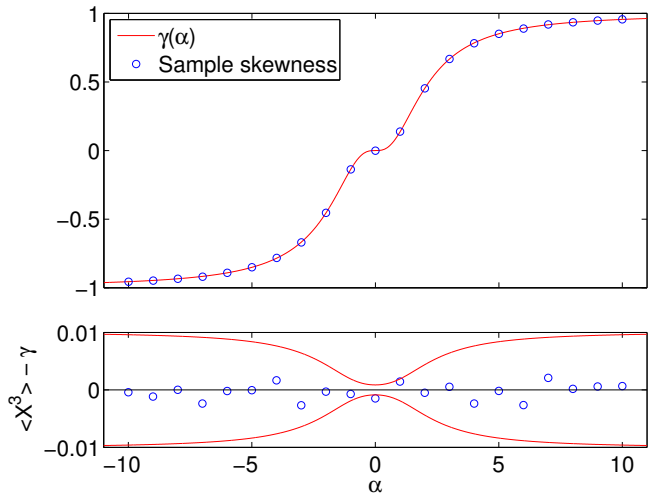

Figure 3.6: Skewness of the same samples as in Fig. 3.4. The top graph shows $\gamma(\alpha)$ along with the average skewness of the samples. The bottom graph shows the deviations from the expected skewness $\gamma(\alpha)$ with red lines indicating one standard deviation as calculated in Appendix A.

Chapter 4

Correlated surfaces

With a working random number generator in place, the next step is to create a realistic surface where the heights are correlated, and not just statistical noise. For this purpose, two algorithms will be presented. The first is called Fourier filtering and provides a simple way of generating signals with any correlation function. The drawback of this method is that it only works for signals with normally distributed amplitudes (i.e. surface heights). This is unfortunate as the explicit purpose of this thesis is to deviate from the normal height distribution to explore the effect of the skewness of the height distribution. However, the Fourier filtering method is central in the algorithm presented by Nichols et al. (in this thesis named only Nichols' algorithm for brevity) [9]. With this algorithm it is possible to generate correlated surfaces using any set of numbers and (in principle) any correlation function. The principles of both methods will be given before the results of the implementation of Nichols' algorithm are presented. To end this Chapter, a brief comparison of the two algorithms is given.

The methods require a discrete Fourier transform, here defined as

$$\hat{x}(k) = \mathrm{FT}(x(j)) \equiv \sum_{j=0}^{N-1} x(j) \exp(-\mathrm{i}2\pi j/N) \tag{4.1}$$

for the forward transform and

$$x(j) = \mathrm{FT}^{-1}(\hat{x}(k)) \equiv \frac{1}{N} \sum_{k=0}^{N-1} \hat{x}(k) \exp(\mathrm{i}2\pi k/N) \tag{4.2}$$

for the inverse.

4.1 Fourier filtering

In Chapter 2 the surface was represented as a set of amplitudes at discrete locations ξ_n along the x_1-axis with amplitudes $\zeta(\xi_n)$. The amplitudes were generated from random, uncorrelated numbers $\{X_n\}$ and a set of weights $\{W_j\}$, written as

$$\zeta(\xi_k) = \sum_{j=-\infty}^{\infty} W_j X_{j+k}. \tag{4.3}$$

The set $\{W_j\}$ is determined by first examining the average height-height correlation

$$\begin{aligned}\langle \zeta(\xi_k)\zeta(\xi_{k+l})\rangle &= \langle \delta^2 \sum_{m=-\infty}^{\infty}\sum_{j=-\infty}^{\infty} W_m W_j X_{m+k} X_{j+k+l}\rangle \\ &= \delta^2 \sum_{m=-\infty}^{\infty}\sum_{j=-\infty}^{\infty} W_m W_j \langle X_{m+k} X_{j+k+l}\rangle. \end{aligned}\tag{4.4}$$

The angle brackets $\langle \cdots \rangle$ denote an average over an ensemble of realizations. The random numbers $\{X_n\}$ are uncorrelated and have a standard deviation of 1, thus

$$\langle X_m X_n\rangle = \delta_{mn}, \tag{4.5}$$

where δ_{mn} is the Kronecker delta. Using this in Eq. (4.4) gives

$$\langle \zeta(\xi_k)\zeta(\xi_{k+l})\rangle = \delta^2 \sum_{j=-\infty}^{\infty} W_j W_{j-l}. \tag{4.6}$$

The Wiener-Khinchin theorem states that the autocorrelation function of a stationary random process has a spectral decomposition given by the power spectrum of that process [5]. The power spectrum was introduced in Chapter 2 as the Fourier transform of the autocorrelation function. Due to the ensemble averaging this process is stationary, and the theorem applies. For this process, this implies

$$\langle \zeta(\xi_k)\zeta(\xi_{k+l})\rangle = \delta^2 \int_{-\infty}^{\infty} \frac{1}{2\pi} \exp(\mathrm{i}Q\xi_l) g(|Q|)\, \mathrm{d}Q, \tag{4.7}$$

where $g(|Q|)$ is the power spectral density given by Eq. (2.7) for the Gaussian case. Next comes a derivation given in Appendix A of Ref. [4]. First, the weights are written as the Fourier transform of some function $\hat{W}(Q)$, yielding

$$W_j = \int_{-\infty}^{\infty} \frac{1}{2\pi} \hat{W}(Q) \exp(\mathrm{i}Q\xi_j)\, \mathrm{d}Q. \tag{4.8}$$

Using

$$\sum_{j=-\infty}^{\infty} f(\xi_j) = \frac{1}{\Delta x} \int_{-\infty}^{\infty} f(\xi)\, \mathrm{d}\xi \tag{4.9}$$

in the limit $\Delta x \to 0$, Eqs. (4.6) and (4.7) give

$$\frac{1}{\Delta x} \int_{-\infty}^{\infty} \frac{1}{2\pi} \hat{W}(Q)\hat{W}(-Q) \exp(\mathrm{i}Q\xi_l)\, \mathrm{d}Q = \int_{-\infty}^{\infty} \frac{1}{2\pi} g(|Q|) \exp(\mathrm{i}Q\xi_l)\, \mathrm{d}Q. \tag{4.10}$$

Assuming that $\hat{W}(Q)$ is real, Eq. (4.10) gives

$$\hat{W}(Q) = (\Delta x)^{1/2} g^{1/2}(|Q|), \tag{4.11}$$

which can be substituted into Eq. (4.8) to give

$$W_j = (\Delta x)^{1/2} \int_{-\infty}^{\infty} \frac{1}{2\pi} g^{1/2}(|Q|) \exp(\mathrm{i}Q\xi_j)\, \mathrm{d}Q. \tag{4.12}$$

This is in principle enough to calculate the weights and generate randomly rough surfaces. However, a special case occurs if the random numbers X_n have a normal distribution. As the Fourier transform of a Gaussian function is a Gaussian function itself, a set of Gaussian numbers $\{X_j\}$ can be used as both in the frequency domain and spatial domain without actually performing a Fourier transform. As Eq (4.12) is a Fourier transform of the square root of the power spectral density, Eq (4.3) can be viewed as a convolution of $\sqrt{g(k)}$ and $\{X_j\}$. Hence, the following algorithm is obtained for generating surfaces of length L with power spectral density $g(k)$ from a set of N random Gaussian uncorrelated numbers $\{X_j\}$:

1. Assign $\{X_j\}$ to the locations $\xi_j = j\Delta x_1$, with $j = 0, 1, 2, \ldots, (N-1)$ and $\Delta x = L/N$. This is the initial surface $y(\xi_j)$.

2. Sample $g(k)$ at discrete frequencies $k_n = (n - N/2)\Delta k$, where $\Delta k = 2\pi/L$ and $n = 0, 1, 2, \ldots, (N-1)$.

3. Calculate the Fourier transform $\hat{y}(k_n) = \mathrm{FT}(y(\xi_j))$.

4. Calculate $\hat{\zeta}(k_n) = \hat{y}(k_n) \cdot (g(k_n))^{1/2}$.

5. Generate the surface in real space via the inverse discrete Fourier transform $\zeta(\xi_j) = \mathrm{FT}^{-1}(\hat{\zeta}(k_n))$.

The surface $\{\zeta(\xi_j)\}$ now has the height-height correlation corresponding to the power spectral density $g(k)$. Unfortunately, the assumption of normal height distribution has been made to get to this point. If this algorithm is used on any

other height distributions, the surface is whitened by the process, which means that the heights tend towards a normal distribution. The driving force behind this process is the central limit theorem, hence the effect is stronger for large values of N. This effect was discovered when attempts were made to generate surfaces with a skew normal height distribution and the resulting height distributions had lost up to 50% of their original skewness. In effect, Fourier filtering is an excellent way of generating correlated surfaces, but only as long as the target height distribution is a normal distribution.

4.2 Nichols' algorithm

Nichols et al. proposed a simple solution to this problem which allows the combination of, in principle, any height distribution with any correlation function [9]. The only limitation mentioned is that sharp peaks in the power spectral density are not compatible with strongly asymmetrical height distributions. The example given is trying to combine an exponential height distribution with a narrow band pass filter as correlation function. Such special cases are rare, and this limitation is not a problem in the context of this work. The method works by iteratively reordering the original data and using Fourier filtering to determine the reordering process. As the resulting surfaces are comprised of the exact data points of the original signal, the generated surfaces are guaranteed to have the correct height distribution. The algorithm to generate a surface with length L and power spectral density $g(k)$ from a set of N random uncorrelated numbers $\{X_j\}$ is as follows:

1. Assign the N random numbers $\{X_j\}$ to the locations $\xi_j = j\Delta x$ with $j = 0, 1, \ldots, N-1$ and $\Delta x = L/N$. This is the initial surface $y(\xi_j)$.
2. Store a copy of $y(\xi_j)$ in a vector $s(j)$ and sort by ascending value. Hence, the smallest value in $y(\xi_j)$ is stored in $s(1)$, the second smallest value in $y(\xi_j)$ in $s(2)$ and so on, such that $s(1) \leq s(2) \leq \ldots \leq s(N)$.
3. Sample $g(k)$ at discrete frequencies $k_n = (n - N/2)\Delta k$, where $\Delta k = 2\pi/L$ and $n = 0, 1, \ldots, N-1$.
4. Calculate the Fourier transform $\hat{y}(k_n) = \mathrm{FT}(y(\xi_j))$.
5. Find the phases $\phi(k_n) = \tan^{-1}\left(\frac{\mathrm{Im}(\hat{y}(k_n))}{\mathrm{Re}(\hat{y}(k_n))}\right)$.
6. Calculate $\hat{\zeta}(k_n) = \exp(\mathrm{i}\phi(k_n))(g(k_n))^{1/2}$.
7. Generate the surface in real space via the inverse Fourier transform: $\zeta(\xi_j) = \mathrm{FT}^{-1}(\hat{\zeta}(k_n))$.

8. Replace the values of $\zeta(\xi_j)$ with the values stored in $s(j)$, replacing the smallest value of $\zeta(\xi_j)$ with $s(1)$, the second smallest in $\zeta(\xi_j)$ with $s(2)$ and so on. As the numbers are replaced, keep record of the position at which each element of $s(j)$ is stored in $\zeta(\xi_j)$.

9. If all the numbers in $s(j)$ are assigned the same position as the last iteration, the algorithm is terminated with $\zeta(\xi_j)$ as the resulting surface. Otherwise, steps 4-9 are repeated, replacing $y(\xi_j)$ with the current surface $\zeta(\xi_j)$ in step 4.

In the original algorithm the mean of $y(\xi_j)$ is removed in the beginning and reinserted at the end, and the variance of $y(\xi_j)$ is scaled by the variance of $g(k)$. This is not strictly necessary here, as the mean and variance of $y(\xi_j)$ are close to 0 and 1, respectively, and $W(x_1)$ is normalized. Note that step 6 is essentially a Fourier filtering process, as it combines the amplitudes of $g(k_j)$ with the phases of the Fourier transform of the underlying numbers. After the inverse transform in step 7 the surface has the correct correlation, but the height distribution is whitened. Step 8 corrects this by replacing the height distribution with the original values, which in turn affects the height-height correlation.

This algorithm is essentially the solution to a optimization problem, where a set of numbers are to be reordered to approximate a target autocorrelation function. The problem always has at least two solutions, as mirroring the surface about $x_1 = L/2$ gives the same autocorrelation. It is not known whether there may be more solutions, and if there are, whether the algorithm finds the global optimum. Santos and Yacoub were able to show that the algorithm converges asymptotically to the correct power spectral density as N becomes large [10]. However, several adjustments were necessary in order to make the algorithm work in practice, including making sure that the algorithm is not caught in an infinite loop in steps 4-9. Details on these adjustments and their effect on the surfaces are given in Section 5.3.

Nichols' algorithm was implemented using Fortran 90, and an implementation of the Quicksort algorithm[1] written by Juliana Rew[2] was used to sort the numbers. This code was modified to also keep track of the indices of the sorted numbers in order to terminate the surface generation algorithm after convergence is achieved.

4.3 Results and discussion

Results from testing of Nichols' algorithm are presented in Figs. 4.1-4.3. Figure 4.1 shows surface realizations for different values of the skewness parameter

[1] `http://www.fortran.com/qsort_c.f95`

[2] `http://www.cisl.ucar.edu/staff/juliana/`

α, demonstrating the qualitative impact of the surface height skewness. Figure 4.2 shows the corresponding average height histograms and height-height correlation functions for $N_\zeta = 1000$ surface realizations as well as their target (analytical) functions. The parameters for the surfaces are length $L = 10\,\mu$m, correlation length $a = 2\mu$m and RMS roughness $\delta = 1\mu$m, and they were disctretized using $N = 4096$ data points. As $\Delta x_1 = L/N = 2.44\,\text{nm} \ll a$, the details in the surfaces are well resolved. Figure 4.3 shows surface realizations and average correlation functions for $\alpha = 7$ and different values of a.

The surfaces in Fig. 4.1 look mostly smooth and well behaved, but they all have a few very sharp peaks and troughs. Examples are found near $x_1 = 1.5\,\mu$m for both $\alpha = 7$ (top) and $\alpha = -7$ (bottom). Even in the Gaussian case in the middle surface there is a sharp downward spike near $x_1 = -3.5\,\mu$m and an upward spike near $x_1 = 0.5\,\mu$m. These spikes are a direct consequence of using Nichols' algorithm. If a statistical outlier is generated in the original set of random numbers, it will need to be put somewhere in the resulting surface. This can result in very sharp peaks, which in turn leads to extremely large local derivatives. The first and second derivatives are used in the simulations in Chapter 5, where the necessity of smoothing the surfaces will be demonstrated.

As Nichols' algorithm reorders the original data, the histogram plots in Fig. 4.2 are equivalent to those shown in Section 3.3. The histograms are included here as well for completeness and as an additional visualization of the impact of the skewness parameter on the surface realizations. The average autocorrelation functions in the left column of Fig. 4.2 are very close to their targets, but it is worth noting that there is a small anticorrelation $\langle \zeta(x_1)\zeta(x_1')\rangle < 0$ for $|x_1 - x_1'| > 200\,\text{nm} = 2a$. However, the correlation function, including this anticorrelation, is consistent for different values of α, thus the main objective of testing the effect of height distribution skewness on the scattering process can still be accomplished. To ensure consistent correlation, one should take care to use Nichols' algorithm also for the special case of $\alpha = 0$, even though it might be tempting to use the more efficient Fourier filtering.

As expected, the surfaces get more 'spiky' as $|\alpha|$ increases. Note that the skewness for $\alpha = 7$ is $\gamma(\alpha) = 0.917$, which is fairly close to $\gamma_{max} \simeq 0.995$ (with corresponding negative numbers for $\alpha = -7$). In other words, surfaces with a skew normal height distribution cannot be much more 'spiky' than the top and bottom surface in Fig. 4.1. It is also worth pointing out that due to a large ratio between the RMS roughness δ and the correlation length a (in Figs. 4.1 the ratio is $\delta/a = 10$) these surfaces have very steep features compared to what is usually used for simulation purposes. An experimental measurement of a real surface by Simonsen et al. found $\delta/a = 0.04\,\mu\text{m}/1.3\,\mu\text{m} = 0.03$ [11], and simulations in the review by the same author frequently uses a ratio of $\delta/a \simeq 0.5$ [1].

Figure 4.3 shows plots of generated and target correlation functions as well

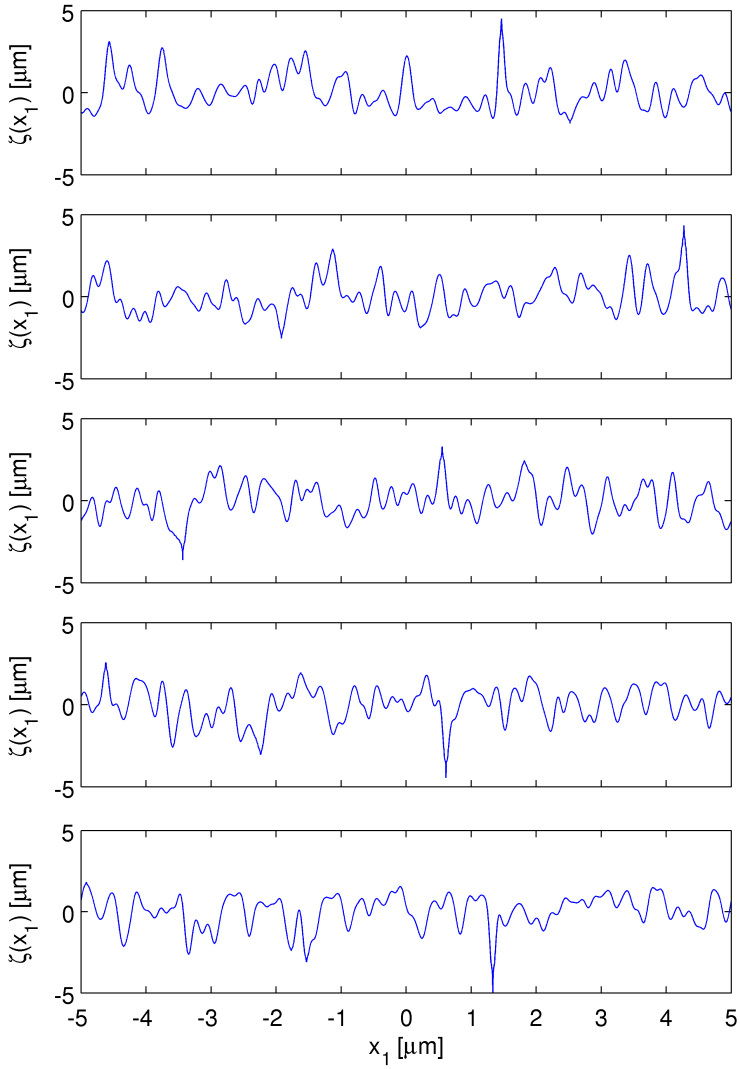

Figure 4.1: Surface realizations for different values of α. From top to bottom the values of α are 7, 3, 0, -3 and -7, respectively, and the corresponding skewnesses in μm are 0.917, 0.667, 0, -0.667 and -0.917. The other parameters were length $L = 10\,\mu$m, RMS roughness $\delta = 1\,\mu$m and correlation length $a = 100\,$nm for all the realizations.

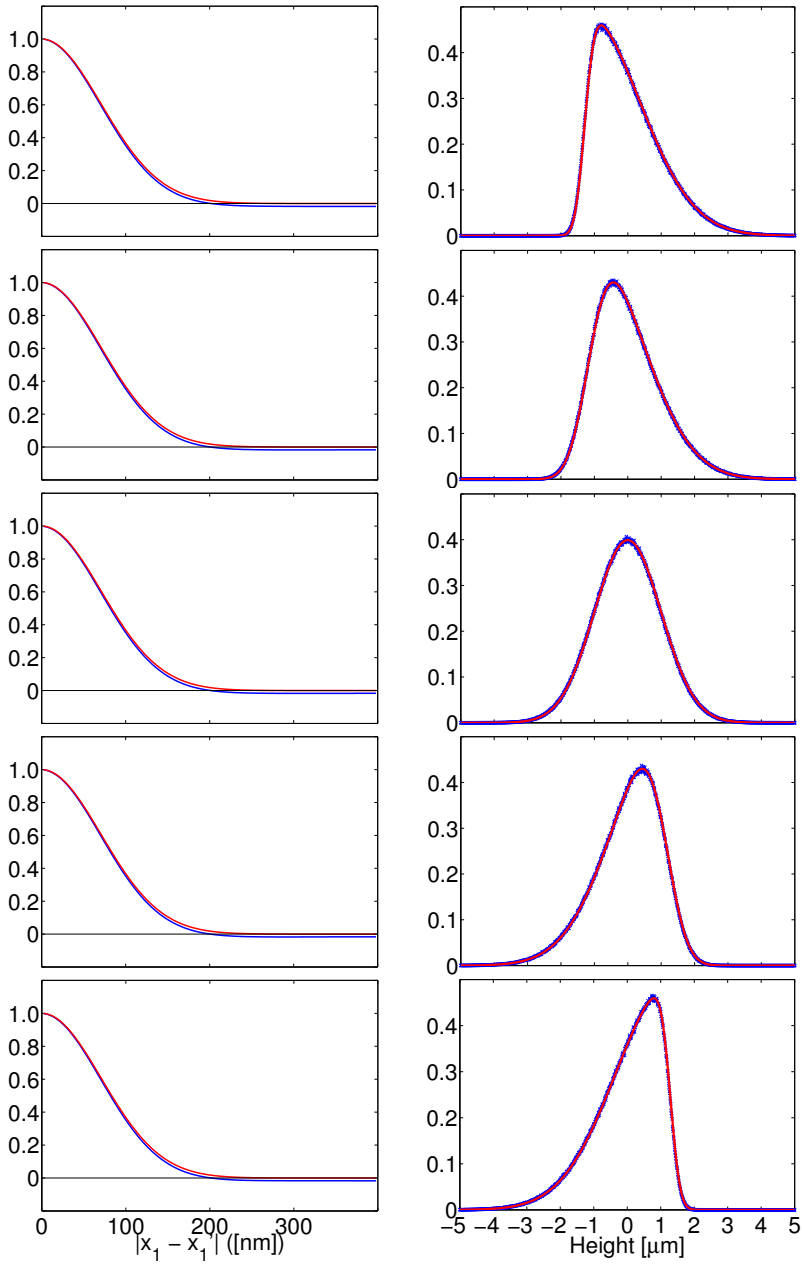

Figure 4.2: Left column: Average correlation functions (blue) compared to the target (red) for the corresponding values of α as in Fig. 4.1. Right column: Surface height histograms (blue crosses) and target height distribution (red) for the same values of α. The sample size was $N_\zeta = 1000$ surfaces and the other parameters are the same as in Fig. 4.1.

as a surface realization like those shown in Figs. 4.1 and 4.2, but for varying correlation lengths a. It appears that the weak anticorrelation is dependent on a: larger correlation lengths give larger anticorrelation. The transition from correlation to anticorrelation happens at $|x_1 - x_1'| \simeq 2a$. These results show that the problem of anticorrelation that arise from using Nichols' algorithm can be minimized by choosing a large system length L compared to the correlation length a. The anticorrelations for large distances $|x_1 - x_1'|$ seen in Fig. 4.3 are around -0.007, -0.015 and -0.033 for $a = 50\,\text{nm}$, $a = 100\,\text{nm}$ and $a = 200\,\text{nm}$, respectively. This implies that the ratio a/L should not exceed 0.01, which is the ratio in the middle plot. If this is not possible for the system to be simulated, an overhead factor can be used. In this case, a surface of length mL is generated using mN data points, before a section of N data points is extracted. The overhead factor m should be chosen such that $mL \geq 100a$. In Section 5.3 it is demonstrated that an overhead factor was necessary for other reasons as well.

The surface realizations show how the correlation length a affects the structure of the surface. Note that the surfaces are generated from the exact same data points, only rearranged to give the appropriate autocorrelation. Again one typical consequence of using Nichols' algorithm is apparent: an outlier with a value of almost $\zeta(x_1) = 5\,\mu\text{m}$ has been generated with few data points with similar values. This data point still has to be placed somewhere, which gives a very sharp spike near $x_1 = -1\,\mu\text{m}$ both for $a = 100\,\text{nm}$ and $a = 200\,\text{nm}$. (The data point is also found near $x_1 = 4.5\,\mu\text{m}$ for $a = 50\,\text{nm}$, but the impact is less pronounced as the short correlation length gives a very spiky surface in general.)

4.3.1 Fourier filtering and Nichols' algorithm: a brief comparison

The biggest advantage of using Nichols' algorithm is clear: it allows the combination of any height distribution with any autocorrelation function. It is also clear that this algorithm gives the correct height distribution, as the resulting surface has the exact same height distribution as the input. The results have already shown two drawbacks: the surfaces show a weak anticorrelation for $|x_1 - x_1'| > 2a$ when a/L is larger than about 100, and outliers in the input data give sharp peaks in the surfaces resulting in large local derivatives. These problems will be addressed in Section 5.3.

Another drawback is the issue of computational cost. Each iteration in Nichols' algorithm involves a forward and backward Fourier transform plus a sorting of the signal in order to replace the whitened signal with the original data points. Efficient implementations of Fourier transform and sorting algorithms both require $O(N \log(N))$ operations (on average). The effect of N on the number of iterations required by Nichols' algorithm was not investigated, but

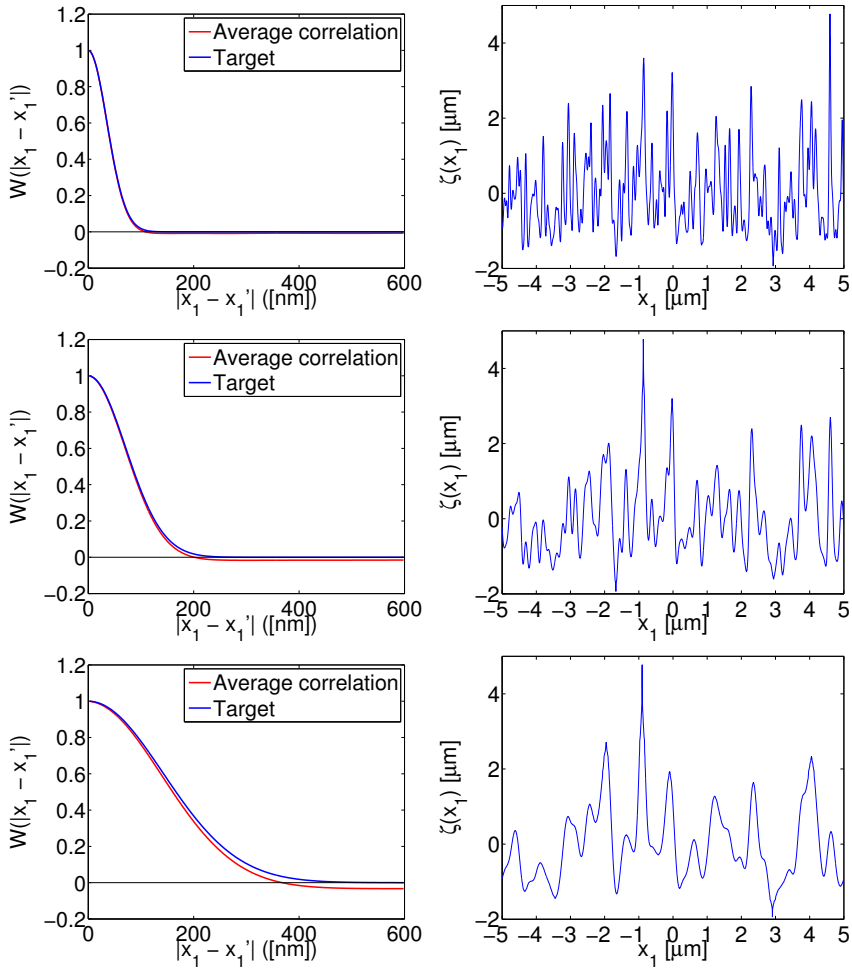

Figure 4.3: Results of surface generator testing using Nichols' algorithm. The left column shows the average empirical correlation compared to the target. The right column shows a surface realization with the corresponding correlation function. The correlation lengths for the top, middle and bottom plots were $50\,\mathrm{nm}$, $100\,\mathrm{nm}$ and $200\,\mathrm{nm}$, respectively. The surface parameters are length $L = 10\,\mu\mathrm{m}$, rms-height $\delta = 1\,\mu\mathrm{m}$ and skewness parameter $\alpha = 7$. They were discretized with 4096 points, and the autocorrelations were averaged over 1000 surfaces. The three surface realizations were generated from the exact same vector of data points, only reordered to give the appropriate correlation.

it is natural to assume that larger N require more iterations. The advantage of the Fourier filtering algorithm its effectiveness: it requires fewer operations than a single iteration of Nichols' algorithm as it only needs the Fourier transforms. In addition, the resulting surfaces are significantly smoother. However, it only works for Gaussian height distributions.

A last potential advantage for Fourier filtering is that it has been shown to work for two-dimensional surfaces. Although there are no apparent reasons Nichols algorithm should not work by simply performing Fourier filtering and data substitution for two dimensions, this has not been tested and it is possible that practical problems can arise.

Chapter 5

Numerical simulations

Keeping in mind that the main task of this thesis is studying the effect of surface height skewness on scattering processes, it is clear that the height distribution and surface generator described in the previous two Chapters provide the necessary tools. The skewness of the height distribution can be altered via a skewness parameter α while keeping the mean and variance constant, and the surface generator reorders an input of random numbers to create surfaces with a constant autocorrelation. This allows simulations where only the skewness is varied while the other statistical properties of the surfaces are equal. The surface generator was integrated in the code of Maxwell1D, a Fortran 90 program created by I. Simonsen designed to simulate one-dimensional rough surface scattering. Both the theory behind this program and its implementation is beyond the scope of this work, and the interested reader is again referred to Ref. [1]. However, subjects relevant to this thesis will be explained, such as input parameters, output parameters and a few scattering phenomena. In addition, simulation results showed that the surfaces had to be filtered, and the method and results of this filtering will be presented.

5.1 Geometry and input parameters

The geometry of the scattering process is shown in Fig. 5.1. An electromagnetic beam of light with wavelength λ and finite width g is incident on an interface between two media. (Note that g is different from the power spectrum $g(k)$. The notation follows the convention in the literature.) The polarization of the incident field will be specified as either p-polarized (parallel to the plane of incidence spanned by x_1 and x_3) or s-polarized (perpendicular to the plane of incidence). The medium above the interface is a vacuum with dielectric constant $\varepsilon_0(\omega) = 1$,

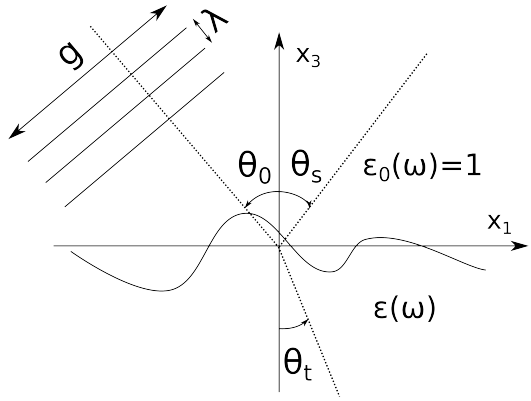

Figure 5.1: Sketch of the scattering geometry. The lengths λ and g and the size of the height fluctuations are not to scale. Notice the directions for which the different angles are defined positive.

and the medium below has a complex dielectric constant $\varepsilon(\omega)$. The interface is the surface $\zeta(\xi_1)$ from the rough surface generator. In practical applications the beam width g is often negligible compared to the surface length L, but in simulations L must have a finite size. Here a compromise must be found: if $L \simeq g$ (or smaller) computational artefacts such as lost energy at the edges may occur, but increasing the system size (i.e. the number of discretization points along x_1) has a significant computational cost. A reasonable compromise for the Maxwell1D program is $L \simeq 4g$.

For an incident beam characterized by the parameters g, λ and θ_0 the field along the surface is calculated and the outgoing field is calculated for θ_s discretized on the interval $(-90°, 90°)$. The standard input parameters given in Table 5.1 will be used unless specified otherwise. The overhead factor m will be explained in Subsection 5.3.1. For the standard parameters $|\mathbf{k}|\delta = (2\pi/0.6127\,\mu\text{m}) \cdot 1\,\mu\text{m}$, and the surfaces are rough according to the Rayleigh criterion given in Eq. (2.2) for angles of incidence up to $\theta_0 = 86°$.

5.2 Output parameters

The relevant output parameters from Maxwell1D are unitarity, coherent fraction of the total scattering and mean differential reflection coefficient (MDRC) for opaque (non transparent) materials, and mean differential transmission coefficient and transmittance for transparent materials.

Unitarity is the ratio between the incoming and the outgoing energy and is a

Table 5.1: Standard parameters used in simulations, unless specified otherwise.

Parameter	Symbol	Value
Surface length	L	$25.6\,\mu$m
RMS roughness	δ	$1\,\mu$m
Correlation length	a	$2\,\mu$m
Wavelength	λ	$0.6127\,\mu$m
Beam width	g	$6.217\,\mu$m
Discretization	Δx_1	$0.06217\,\mu$m
Number discretization points along θ_s and θ_t	N_θ	501
Number of realizations	N_ζ	10000
Overhead factor	m	20

first measure of the consistency of the simulation. If the medium is non absorbing (i.e. $\mathrm{Im}(\varepsilon(\omega)) = 0$), the unitarity should ideally be exactly 1. Figure 5.2 shows the unitarity of a flat surface without absorption as a function of the angle of incidence θ_0. There are already computational artefacts, as the unitarity is 1-2% too low for $\theta_0 = [0°, 70°]$ in p-polarization and 1-2% too high in s-polarization. If $\theta_0 = 80°$ the unitarity suddenly drops for both polarizations. For this work θ_0 will be restricted to the interval $[0°, 60°]$. Note that the unitarity converges after a few samples, so the standard 10 000 are not needed here. For media with $\mathrm{Im}(\varepsilon(\omega)) > 0$ the unitarity should be a number on the interval $(0, 1)$ and is used to measure the absorption in the medium.

The coherent fraction of the total scattering states how much of the scattered intensity which was scattered non-diffusely, as discussed in Chapter 2.1 and illustrated in Fig. 2.1. This will be a number between 0 (strongly rough surface) and 1 (flat surface). Note that the coherent component is not the same as the scattered intensity in the specular direction, but in a lab experiment it is not possible to distinguish the coherent and incoherent components.

The mean differential reflection coefficient (MDRC) is the reflected intensity as a function of the scattering angle θ_s. It is denoted as $\langle \partial R_p/\partial\theta_s \rangle$ for p-polarization and $\langle \partial R_s/\partial\theta_s \rangle$ for s-polarization. The MDRC is linked to the unitarity: the total area under the curve of the MDRC is equal to the unitarity for non absorbing materials. Unlike the unitarity, the MDRC converges slowly, and is the reason why 10 000 samples are used. The program Maxwell1D also allows the separation of the coherent and incoherent parts of the scattered intensity instead of looking at the total intensity. The coherent fraction of the total scattering is again linked to the coherent component: it is equal to the total area under the curve of the coherent component.

For certain parameters, the MDRC demonstrates a phenomenon called enhanced backscattering. This is a multiple scattering phenomenon that arises

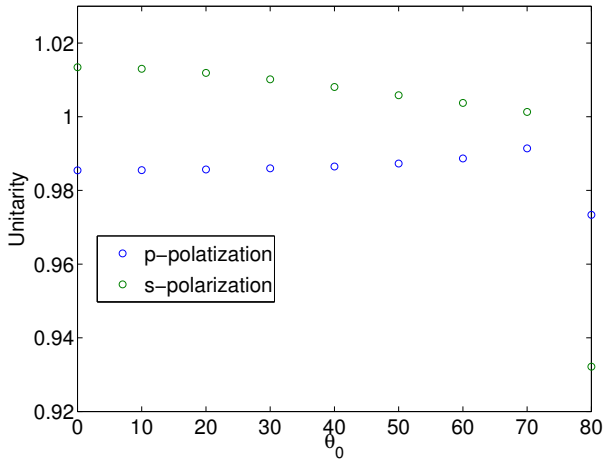

Figure 5.2: Unitarity of flat surfaces, calculated using $N_\zeta = 500$ realizations, RMS roughness $\delta = 0.00001$ and $\varepsilon(\omega) = -17.2$ (no absorption). The other parameters are given in Table 5.1.

from the constructive interference of double scattering paths and is a signature of rough surfaces. An illustration of double backscattering paths is shown in Fig. 5.3. Two incoming parallel rays are scattered twice at the same locations. If $\theta_0 \neq -\theta_s$, the path lengths are different and thus the phases are in general different. The waves travelling along the paths will hence not interfere constructively in general. However, if $\theta_0 = -\theta_s$, the path lengths, and thus the phases, are the same, and the waves interfere constructively. If $-\theta_s$ is close to θ_0, there is still constructive interference, albeit to a lesser extent. This gives rise to an enhanced backscattering peak in the MDRC around $\theta_s = -\theta_0$. The enhanced backscattering phenomenon was experimentally confirmed by Méndez and O'Donnell in 1987 [12].

Figure 5.4 shows an example of a single sample of the differential reflection coefficient (left) and the average of $N_\zeta = 10\ 000$ samples (right). The single sample has a large component near the specular direction $\theta_s = 20°$. Around this peak there are random fluctuations in the intensity. These are characteristic of scattering patterns from randomly rough surfaces and are called speckles. The MDRC (right) shows a clear example of an enhanced backscattering peak in the direction of the source at $\theta_s = -20°$.

The mean differential transmission coefficient (MDTC) is the equivalent to the MDRC, but for transmission angles θ_t (c.f. 5.1). Naturally, it is non-zero only for

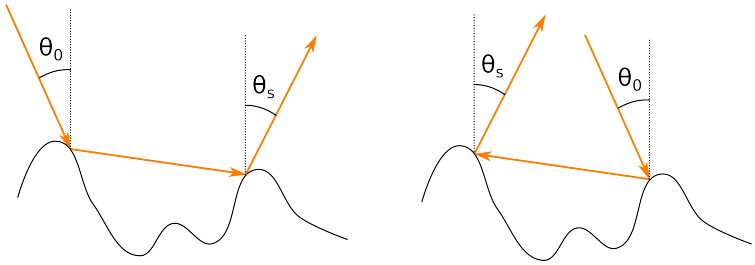

Figure 5.3: Illustration of double backscattering paths. The paths interfere constructively when $\theta_s = -\theta_0$.

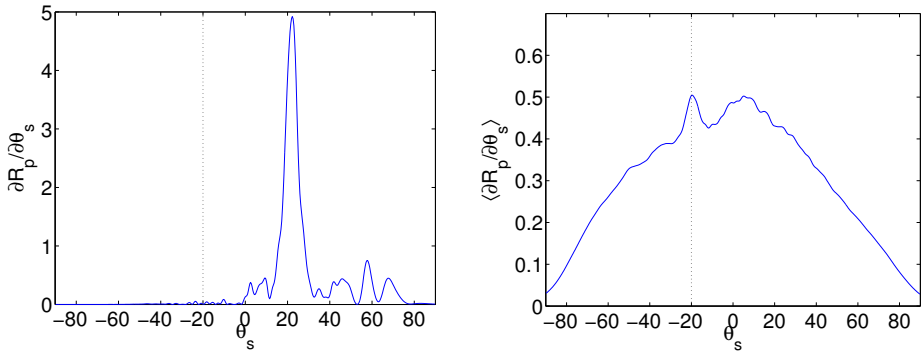

Figure 5.4: Example of single sample differential reflection coefficient (left) and mean differential reflection coefficient (MDRC) from $N_\zeta = 10\ 000$ samples (right). Both scattering patterns are from surfaces with a Gaussian height distribution. The angle of incidence $\theta_0 = 20°$ is indicated by the dashed lines. Note the difference in scale on the y-axis. The dielectric constant was $\varepsilon(\omega) = -17.2 + 0.498\mathrm{i}$ (silver, [13]), and the other parameters are given in Table 5.1.

transparent materials ($\mathrm{Re}(\varepsilon(\omega)) > 0$). It is denoted $\langle \partial T_p/\partial\theta_t \rangle$ for p-polarization and $\langle \partial T_s/\partial\theta_t \rangle$ for s-polarization.

Transmittance is the ratio between the incoming energy and the transmitted energy for transparent materials. For non absorbing materials (i.e. $\mathrm{Im}(\varepsilon(\omega)) = 0$) the sum of the transmittance and reflectance is equal to the unitarity and ideally 1. Hence, the transmittance also gives an indication of the size of the reflectance. The transmittance and the MDTC are also linked as the transmittance is the area under the curve of the MDTC.

5.3 Nichols revisited: Practical adjustments

For the numerical simulations used in this work, it turned out that the surfaces needed to be a lot smoother than the ones shown in Chapter 4. If the local derivatives become very large at some location the electromagnetic field will diverge. This in turn "lights up" the rest of the surface, so large local derivatives at a few locations affect the whole surface. Ultimately this resulted in unitarites as large as 1.3 and MDRCs for the special case of normally distributed heights that did not adequately approximate those from surfaces generated with the Fourier filtering method. Such unitarities are clearly unacceptable, as this implies the creation of energy (30% more energy out than in). Nichols' algorithm is constrained to only use the original data, and this turned out to give very large and noisy local derivatives, as will be demonstrated in Subsection 5.3.2. In this Section two adjustments to Nichols algorithm are outlined, and their impact on the surface statistics is shown.

5.3.1 Overhead factor

The first adjustment was using a overhead factor for generating the surfaces. This was briefly mentioned in Sec. 4.3 as a method to avoid anticorrelation in cases where the ratio a/L is too large. To generate a surface of length L using N data points, one instead generates a surface of length mL using mN data points. Afterwards, a section of length L comprised of N data points is extracted. The effect of this, in addition to reducing anticorrelation, is that the algorithm has a larger 'pool' of random numbers to choose from, so that peaks caused by outliers can be smoothened by placing less extreme outliers next to them. There is no correct or recommended value for m in general as it will vary depending on the application and input parameters. In particular, the choice of discretization interval Δx_1 will affect the choice of m. The drawback of large overhead factors is the computational cost mentioned in Section 4.3.1. By trial and error a reasonable compromise for the parameters in Table 5.1 was found to be the interval $m = [10, 25]$. (The minimum requirement to avoid anticorrelation was $mL \geq 100a$,

which gives gives a minimum overhead factor of $m = 7.8$ in this case.) Overhead factors of 50 and 100 were tried, but this resulted in very long generation times with little or no effect on the MDRC.

It was also discovered during testing that if the number of data points becomes very large ($mN \sim 20\ 000$), Nichols' algorithm is increasingly likely to halt in an infinite loop where two or more elements are swapped cyclically. The exact cause of this was not investigated, instead the code was modified so that the surface was discarded and a new was generated if it had not converged after 3000 iterations.

To reduce the computational cost of large overhead factors, it is also possible to extract multiple sections of length L. As was demonstrated in Sec. 4.3, the height-height correlation is negligible after about $2a$, hence several surfaces which are statistically independent may be extracted by discarding sections of a few correlation lengths between them. A last note on overhead factors is that they are also used in Fourier filtering. Here a surface of length $2L$ is generated and a section of length L is extracted from the middle to avoid computational artefacts at the edges of the surface.

5.3.2 Wavelet filtering

The first attempt to smoothen the surface and its derivatives further was a Fourier filter which set high frequency components to zero. This proved inefficient, as local first and second derivatives were still extremely large compared to surfaces generated with the Fourier filtering method, and the filtered surfaces were unable to reproduce results produced with the Fourier filtering method. Thus a wavelet filter was applied, which greatly improved the results. Wavelet transforms are similar to the Fourier transform in the sense that a signal is represented as a set of coefficients, and applications for wavelet transforms include data compression and signal analysis. A detailed description will not be given here, but an "engineer's approach" description with examples and code is given in Section 13.10 of Ref. [7].

One of the advantages of wavelets compared to Fourier filters is that while Fourier filters are localized in frequency but not in space, wavelets are localized in both. With a Fourier filter, an attempt to remove high frequency structures may potentially affect the entire surface. A wavelet filter, on the other hand, allows removal of such structures only at the locations where they exist, leaving the rest of the surface virtually unaffected. However, for both filtering methods the correlation length a has a corresponding frequency, and it is extremely important not to filter out frequencies comparable to or larger than this correlation frequency.

Wavelet filtering of an extreme example is shown in Fig. 5.5. Here, a surface has been generated using the parameters in Table 5.1 and skewness parameter $\alpha = 10$. The left column shows the surface, its first derivative and its second

derivative from top to bottom. The right column shows the section of the surface and derivatives indicated by the black boxes. It is immediately apparent that the filtering process has a minimal impact on the surface height distribution and autocorrelation, as the unfiltered and filtered surfaces are so close that the unfiltered surface is hardly visible behind the filtered surface. For a majority of the surface, the derivatives are also very close and the wavelet filter simply removes minor noise. However, an extremely sharp peak has been generated near $x_1 = -4\,\mu$m. The close up (top right) shows that Nichols' algorithm was not able to smooth this peak out, even with an overhead factor of 20. The result is a large and noisy first derivative and a wildly fluctuating second derivative at this peak. The wavelet filtered surface is very close to the unfiltered, but is substantially smoother. This results in smoother, smaller derivatives which are more accurate to the overall trend of the surface. The maximum and minimum values of the second derivative are in this case reduced to about one tenth of their unfiltered value. Although the skewness parameter α and example was chosen specifically to provide a challenge for the filter, the filtering also greatly improves the local derivatives in general. It will be demonstrated shortly that filtering was strictly necessary also for the Gaussian case.

Altering the surface heights affects both the height distribution and autocorrelation of the surfaces. To ensure that the relevant statistics are not altered too much by the filter, 10 000 surfaces were generated using the parameters in Table 5.1 and skewness parameter $\alpha = 10$, and the statistics were calculated both with and without the filter. The height distributions and autocorrelations are shown in Fig. 5.6. The unfiltered and filtered data are hardly distinguishable, despite a huge difference in local derivatives. The changes of surface heights are also insignificant with respect to the total averages of the mean, variance and skewness of the heights of all the sample, as the filtering process changed each of them by less than 0.1%. These results show that wavelet filtering is an excellent way of smoothing the surfaces created by Nichols' algorithm while preserving the height distribution and autocorrelation.

5.4 Reproduction

To test the quality of the generated surfaces, simulations were run in the Gaussian case of $\alpha = 0$ to compare with results from previous work where Fourier filtered surfaces were used. In this Section the results of these simulations are presented, and the necessity of wavelet filtering is demonstrated.

The MDRCs generated from rigorous simulations using the Fourier method, Nichols' algorithm without filtering and Nichols' algorithm with an overhead factor and wavelet filter are shown in Fig. 5.7 as blue, green and red curves, respectively. Most of the MDRCs show a clear backscattering peak at $\theta_s = -\theta_0$,

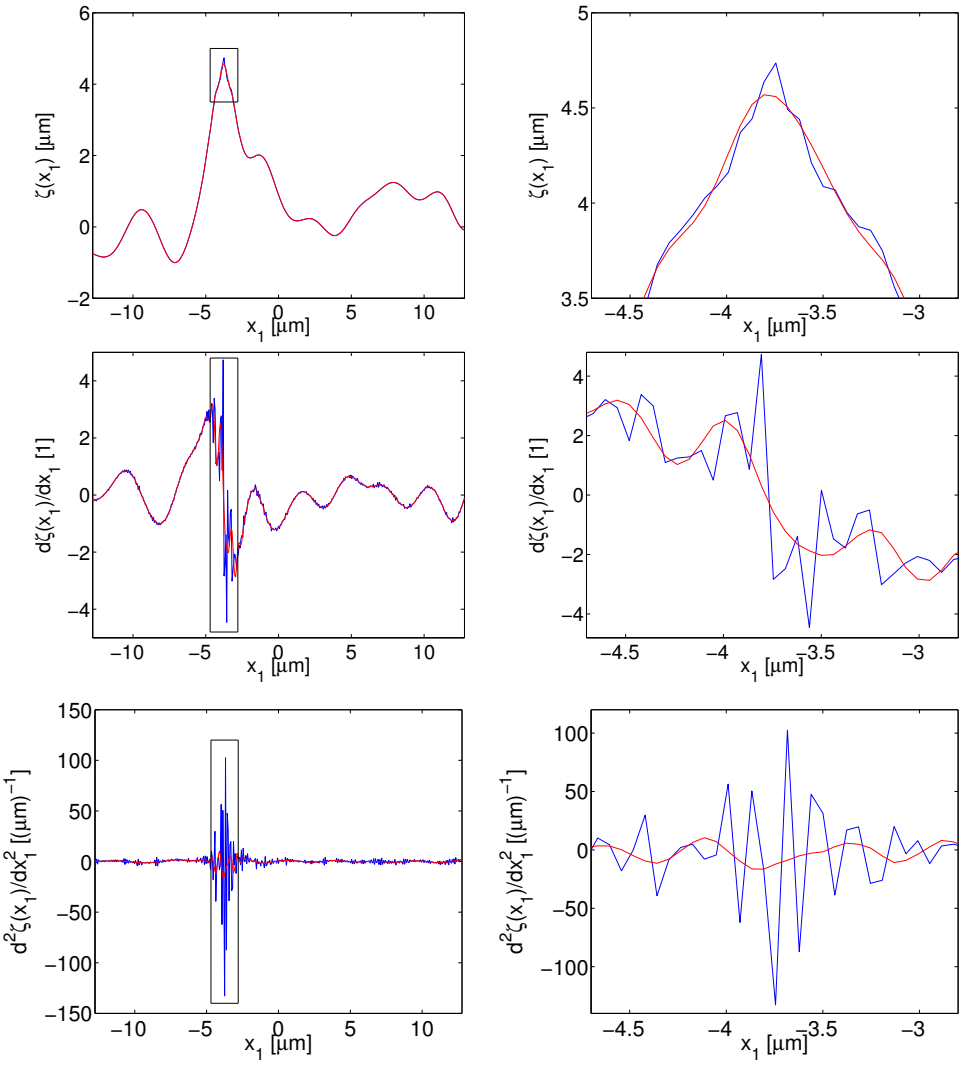

Figure 5.5: Illustration of the effect of wavelet filtering on a surface (top), its derivative (middle) and its second derivative (bottom). The unfiltered realization is shown in blue, while the filtered is shown in red. The left column shows the entire surface, while the right column shows the portions indicated by the black boxes. The surface is generated using the parameters in Table 5.1, skewness parameter $\alpha = 10$ and an overhead factor of 20.

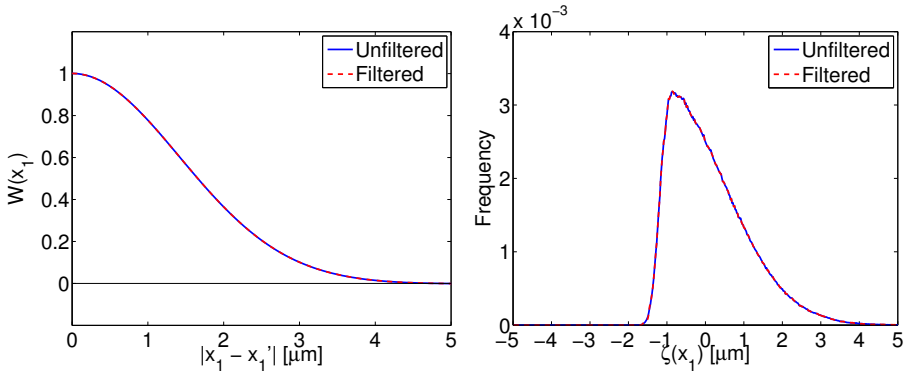

Figure 5.6: Effect of wavelet filtering on surface height statistics and autocorrelation. The filtered and unfiltered data are for the same ensemble of $N_\zeta = 10\ 000$ surfaces generated using the parameters in Table 5.1 and $\alpha = 10$.

Table 5.2: Unitarities for the MDRCs shown in Fig. 5.7.

θ_0 [deg]	Polarization	Fourier	Nichols (filtered)	Nichols (unfiltered)
0	p	0.9463	0.9460	1.2421
20	p	0.9445	0.9448	1.1550
40	p	0.9379	0.9375	1.0871
0	s	0.9982	0.9986	1.0417
20	s	0.9990	0.9985	1.0392
40	s	1.0007	1.0002	1.0404

indicated by the vertical dashed lines. The results for p-polarization immediately show that the unitarities for the unfiltered surfaces are not acceptable, as the area under its curve is substantially larger than that for Fourier filtrated surfaces. The corresponding unitarities for the MDRCs are given in Table 5.2. The results for p-polarization are worse than those for s-polarization due to the fact that the previously mentioned field divergence for large local derivatives only happens with p-polarized light. Although the MDRCs generated for s-polarized light are less noisy, they can hardly be said to reproduce those of Fourier filtered surfaces. For normal incidence ($\theta_0 = 0°$, top right) the MDRC follows the major trends, but it is about 0.05 too high or too low for most angles θ_s. Both for $\theta_0 = 20°$ and $\theta_0 = 40°$, there is a huge dip in the MDRC near the specular directions $\theta_s = 20°$ and $\theta_0 = 40°$, respectively. These dips can also be seen in p-polarization, although it is less apparent due to the fluctuations. All in all, the unfiltered surfaces cannot be said to reproduce the results of Fourier filtered surfaces.

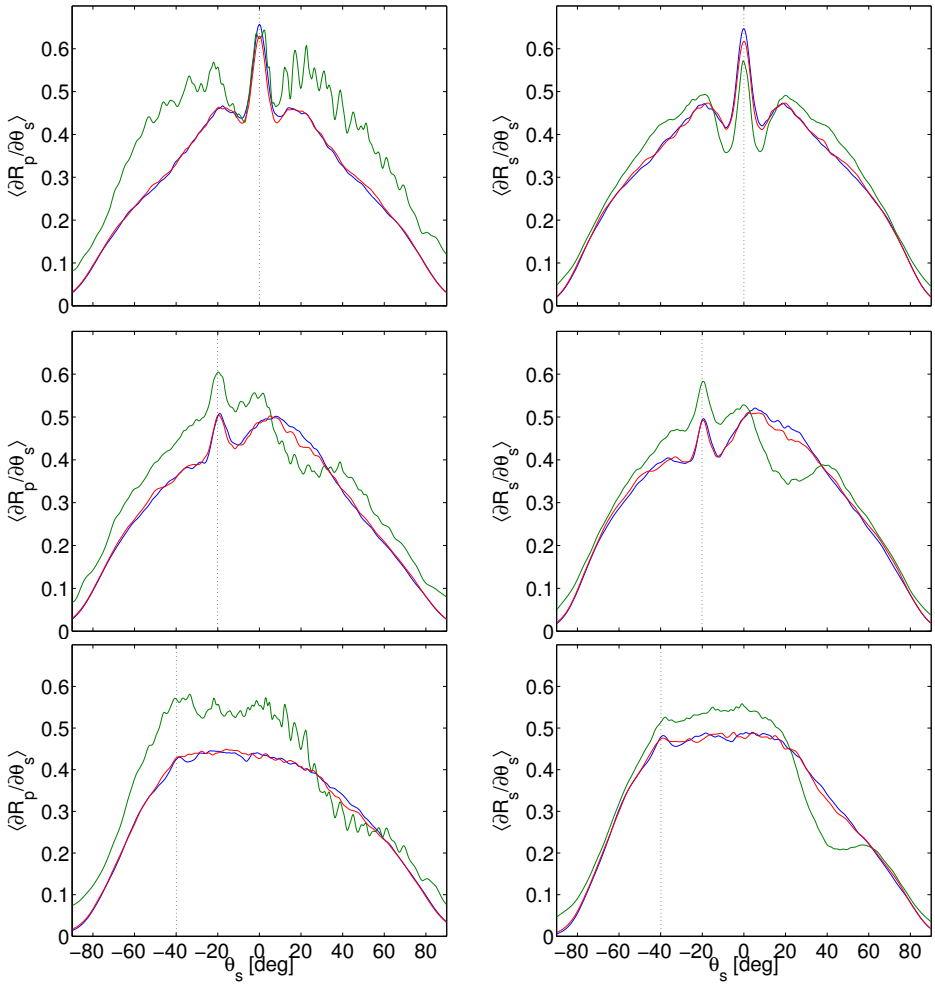

Figure 5.7: Plots of the MDRC as a function of θ_s generated using the parameters in Table 5.1. The left column is for p-polarized light and the right is for s-polarized. The angle of incidence θ_0 was $0°$, $20°$ and $40°$ for top, middle and bottom row respectively, and is indicated as a vertical dashed line. For the blue graphs the Fourier filtering method was used to generate the surfaces, so this represents a target for Nichols' algorithm. For the green graphs Nichols' algorithm was used with an overhead factor of $m = 2$, while for the red the factor was $m = 20$ and the surfaces were filtered using wavelets. The dielectric constant was $\varepsilon(\omega) = -17.2 + 0.498\mathrm{i}$ and the other parameters are given in Table 5.1.

Although the MDRCs generated from filtered surfaces are not perfectly consistent with the ones generated from Fourier filtered surfaces, they are close enough for the purpose of this work. The discrepancies might be reduced by increasing the number of samples N_ζ or the overhead factor m, or by decreasing the sampling interval Δx_1. Naturally, these adjustments all come with a computational cost. As the surface generator adequately reproduces previous work, the next step is to tune the skewness parameter α to study the effect of the skewness of the surface height distribution.

Chapter 6

Results and discussion

Rigorous simulations using the parameters in Table 5.1 on page 29 were run for multiple values of the skewness parameter α. The results will be divided into opaque (non transparent) materials and transparent materials. A material is opaque if $\mathrm{Re}(\varepsilon) < 0$ and transparent if $\mathrm{Re}(\varepsilon) > 0$. The results for the mean differential reflection/transmission coefficient, unitarity, transmittance and coherent fraction of the scattered intensity are shown in this Chapter, and the impact of the surface height skewness $\gamma(\alpha)$ on the scattering process is discussed.

6.1 Opaque materials

For the results in this Section the dielectric constant for silver with a value of $\varepsilon(\omega) = -17.2 + 0.498\mathrm{i}$ was used [13], unless stated otherwise.

6.1.1 MDRC

Figures 6.1 and 6.2 show results for the MDRC for p- and s-polarizations, respectively. There is still some noise around $\theta_s = [-20°, 40°]$ for $\theta_0 = 20°$ and $\theta_0 = 40°$, which could probably be reduced by more samples or a smaller sampling interval Δx_1. However, the results show the overall effect. Note that the blue curves are for Gaussian surfaces and are identical in both columns. The positive skewnesses (left columns in Figs. 6.1 and 6.2) will be discussed first, before they are compared to negative skewnesses.

The top left plot in both Figures show MDRCs for varying positive skewnesses and normal incidence. Although the difference between Gaussian (blue) and strongly skewed (red) surface heights is not large, one of the effects seems to be that increasing skewness reduces the backscattering peak at $\theta_s = 0°$. This

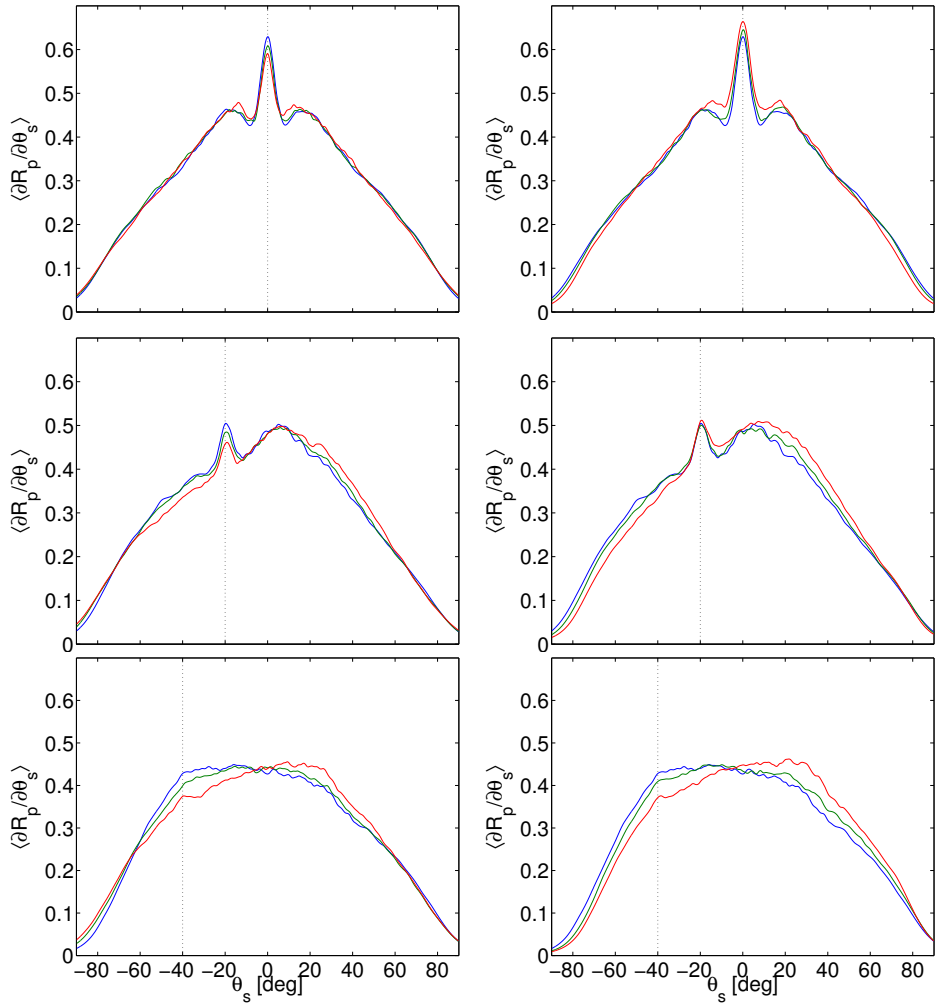

Figure 6.1: MDRC for p-polarization. The left column is for positive skewnesses $\gamma(\alpha)$ with values $\gamma(2) = 0.45\,(\mu\mathrm{m})^3$ (green) and $\gamma(5) = 0.85\,(\mu\mathrm{m})^3$ (red), and the right is for the negative values $\gamma(-2) = -0.45\,(\mu\mathrm{m})^3$ (green) and $\gamma(-5) = -0.85\,(\mu\mathrm{m})^3$ (red). The blue curve is for Gaussian surfaces in both columns. The angles of incidence θ_0 were $0°$, $20°$ and $40°$ for top, middle and bottom row respectively, and are indicated by the vertical dashed lines. The parameters were dielectric constant was $\varepsilon(\omega) = -17.2 + 0.498\mathrm{i}$, length $L = 25.6\,\mu\mathrm{m}$, wavelength $\lambda = 0.6127\,\mu\mathrm{m}$ and correlation length $a = 2\,\mu\mathrm{m}$. The other parameters are given in Table 5.1.

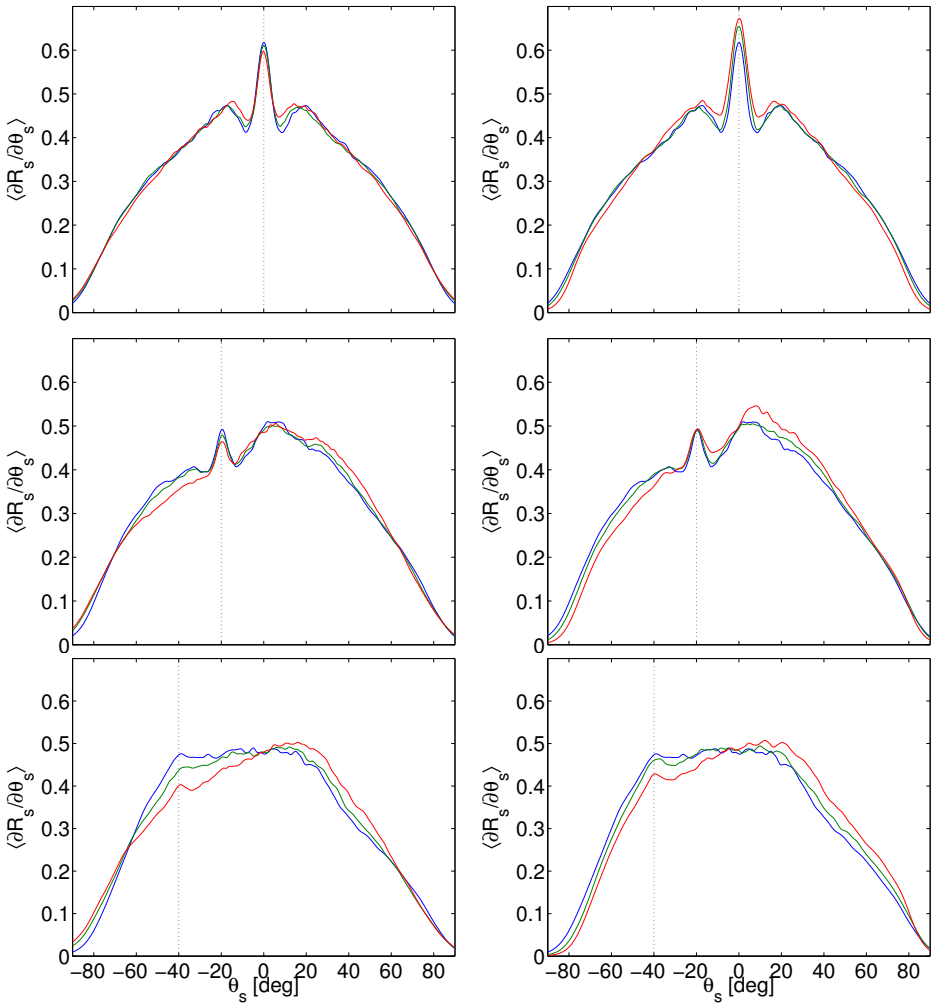

Figure 6.2: Similar to Fig. 6.1, but for s-polarization.

intensity is instead scattered near the local maxima located near $\theta_s = \pm 10°$. The locations of these local maxima are shifted a few degrees towards $\theta_s = 0°$. These locations are related to the average distance between consecutive peaks on the surface, and this shift is similar to the effect of a longer correlation distance a. A possible explanation can be found by realizing that as the surface height skewness increases, the distance between large peaks must also increase. The reason is that as some peak heights increase, others must decrease in order to keep the RMS roughness δ constant. This effect can be seen in Fig. 4.1 by comparing the middle surface ($\gamma(\alpha) = 0\,\mu$m) to the top and bottom surfaces ($\gamma(\alpha) = \pm 0.917\,\mu$m). Hence, the resulting surface effectively has smaller height fluctuations in between sharp peaks, with correspondingly larger distances between the sharp peaks. This argument could explain why the correlation length appears longer than actually it is.

The argument may also be used to explain the differences seen for $\theta_0 = 20°$ and $\theta_0 = 40°$. For $\theta_0 = 20°$ the MDRCs are still very close, but a skewed surface height induces more scattering in the forward direction ($\theta_s > 0$) at the cost of the backward direction. If the sharp peaks are ignored, the rest of the surface looks less rough than a corresponding Gaussian surface, and less rough surfaces scatter more intensity in the specular direction. This is even more apparent in the MDRCs for $\theta_0 = 40°$. Whereas the Gaussian MDRCs (blue) are almost symmetric about $\theta_s = 0°$ in this case, a skewness of $\gamma = 0.85\,\mu$m shifts a significant amount of the scattered intensity from the backward to the forward directions. The difference disappears around $\theta_s = 60°$. This also has an intuitive explanation: if the scattering location is in a 'flat' area in between tall peaks and the scattering angle θ_s is large, there is a large probability that the wave will be scattered again at the next tall peak. After this, it is relatively unlikely to scatter again. Thus, this process reduces the intensity for large θ_s. In addition, the backscattering peak becomes slightly more pronounced as the skewness increases, especially in s-polarization.

From the plots for negative skewnesses (right column in both Figs. 6.1 and 6.2), it is immediately apparent that increasing the magnitude of the surface height skewness produces many of the same effects regardless of its sign. The reason for this is that surfaces with large magnitudes of the surface height skewness look very similar outside the peaks and pits. However, there are a few notable differences in the MDRCs. For $\theta_0 = 0°$ (top), the effect on the backscattering peak is opposite compared to a positive surface height skewness, as a larger negative surface height skewness induces more backscattering instead of less. This is easily explained by looking at the difference of a field scattered from a peak compared to a pit. Both peaks and pits on the surfaces are relatively symmetric with respect to the mean surface normal, due to a symmetric correlation function. At normal incidence, a peak will act as a convex mirror and scatter the

incoming field in all directions. Only a small fraction of the field has a chance to scatter again and hence possibly contribute to enhanced backscattering. By contrast, a pit acts as a concave mirror, and the field scattered in a pit is likely to scatter in it again. As the pit is relatively symmetric with respect to the angle of incidence, the double scattering events that cause the backscattering peaks are very likely compared to a surface peak. By close inspection, the effect of this enlarged backscattering peak is also visible for $\theta_0 = 20^\circ$ (middle) and $\theta_0 = 40^\circ$ (bottom) in both Figs. 6.1 and 6.2.

A second difference is seen for angle of incidence $\theta_0 = 40^\circ$ (bottom) and scattering angles $\theta_s > 60^\circ$. If a wave is scattered with a large scattering angle θ_s, a surface with negative surface height skewness does not have large peaks to stop it. Thus, the scattered wave is allowed to propagate and contribute to a larger intensity also for large scattering angles θ_s.

The arguments given are also consistent with the difference seen for $\theta_s = [-90^\circ, -60^\circ]$. The results show that positive skewness increases the scattering in these directions, while negative skewness decreases it. This can again be explained by the existence of tall peaks for positive skewness, and the lack of such peaks for negative skewness. If the incident field is scattered at an angle $-90^\circ < \theta_s < -60^\circ$ near the top of a tall peak, it is unlikely to scatter again, as this would require a nearby taller peak. Scattering in the backward direction is more likely from 'steep' sections of the surface, i.e. locations where the local first derivative is relatively large. Such sections are found on the left side of peaks and right side of pits. If the incoming field is scattered from the right side of a pit, it will most likely also scatter against the left side of the pit before escaping. On the other hand, if it scatters against a peak, it is comparatively more likely not to scatter again and contribute to the intensity at large negative angles θ_s.

6.1.2 Unitarity

Figure 6.3 shows the calculated unitarities for different values of the surface height skewness. The unitarities for $\theta_0 = 0^\circ$, $\theta_0 = 20^\circ$ and $\theta_0 = 40^\circ$ were calculated for the MDRCs in Figs. 6.1 and 6.2.

The unitarities for p-polarization (left) look fairly constant, i.e. independent of surface height skewness. A notable feature is a spike for all θ_0 at $\gamma(\alpha) = 0.667\,\mu$m. This is believed to be a computational artefact, as it was not present when the data was checked after about 7500 out of 10 000 samples, nor was it present when an overhead factor of $m = 10$ was used. A possible explanation is that a surface may have been generated which the wavelet filter could not make smooth enough. This would cause a field divergence and an increase in the unitarities, as was seen in Section 5.4. This also explains why there is no such spike in s-polarization. There is also a small negative trend for increasing $\gamma(\alpha)$ for all θ_0

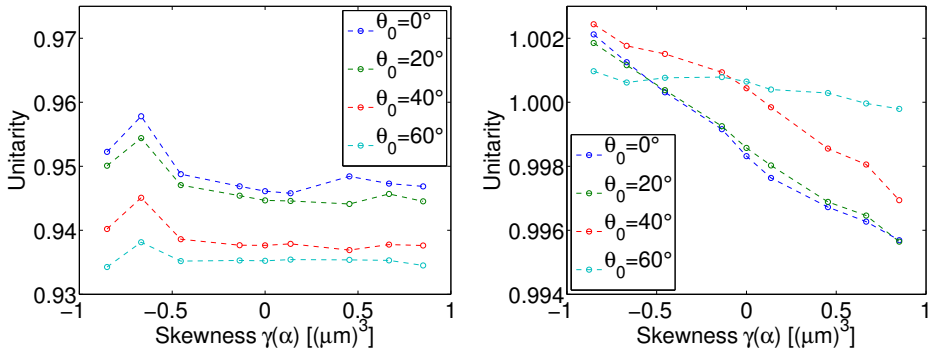

Figure 6.3: Unitarity as a function of surface height skewness for p-polarization (left) and s-polarization (right). The circles represent the data points while the dashed lines are interpolations. The dielectric constant was $\varepsilon(\omega) = -17.2 + 0.498\mathrm{i}$, and the other parameters used are given in Table 5.1.

except $\theta_0 = 60°$. However, the difference from maximum to minimum unitarity (ignoring the spike) is about 0.5% for $\theta_0 = 0°$ and this effect may just as well be a computational artefact.

The unitarities for s-polarization (right) have a clearer trend, but it is very small. The difference between the maximum and minimum unitarities is less than 1% for all θ_0, and the trend may have the same origin as for p-polarization.

As an extra test to see whether there is a correlation between absorption and surface height skewness, simulations were performed with a material with a higher absorption coefficient, i.e. a larger $\mathrm{Im}(\varepsilon(\omega))$. The material chosen was cobalt with dielectric constant $\varepsilon(\omega) = -10.8 + 22.95\mathrm{i}$ for $\lambda = 0.6127\,\mathrm{nm}$ (SOPRA database). Figure 6.4 shows the unitarity as a function of the surface height skewness for p-polarized (left) and s-polarized light. Again, the absorption seems independent of the surface height skewness. One notable exception is $\gamma(\alpha) = -0.85\,\mu\mathrm{m}$ where the rises significantly for all angles of incidence. Although there also seems to be a trend in $\theta_0 = 0°$ and $\theta_0 = 20°$ leading up to this, it is quite possible that it is a numerical artefact as discussed previously.

To summarize, the unitarity cannot be conclusively said to have a dependence on the skewness.

6.1.3 Coherent component

Figure 6.5 shows the coherent fraction of the total scattered intensity as a function of the surface height skewness. For all skewnesses and incident angles θ_0 the fraction is extremely small ($\sim 10^{-4}$), as is expected from strongly rough sur-

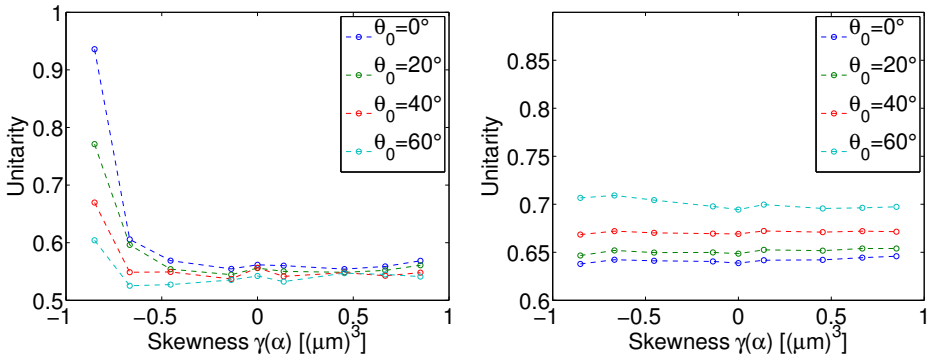

Figure 6.4: Unitarity as a function of skewness with p-polarization (left) and s-polarization (right) calculated using $N_\zeta = 500$ samples. The circles represent the data points while the dashed lines are interpolations. The material was cobalt with a dielectric constant was $\varepsilon(\omega) = -10.8 + 22.95\mathrm{i}$ (SOPRA database), and the other parameters used are given in Table 5.1.

faces. Unlike the unitarities seen in the previous Section, there is no apparent dependence on $\gamma(\alpha)$ (nor θ_0), and the fractions are most likely just noise.

To conduct a better study of the coherent component, simulations using $N_\zeta = 500$ samples, $\delta = 0.2\,\mu$m and the parameters in Table 5.1 were run. For these parameters, the Rayleigh criterion for rough surfaces given in Eq. (2.2) gives $\theta_0 = 40°$. Hence, for the angles of incidence used in these simulations, they are called weakly rough surfaces. The results for the coherent component are shown in Fig. 6.6. The tendency seems to be a slightly larger coherent component for large absolute values of surface height skewness, which is consistent with the argument of a less rough surface in between large peaks and pits for large $|\alpha|$. However, as the effect is fairly small, this should be investigated further before a conclusion is drawn.

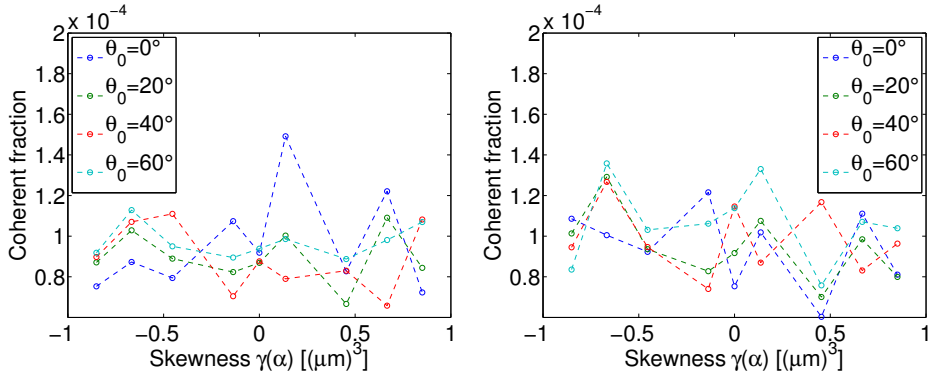

Figure 6.5: Coherent fraction of the scattered intensity for p-polarization (left) and s-polarization (right). The circles represent the data points while the dashed lines are interpolations. The dielectric constant was $\varepsilon(\omega) = -17.2 + 0.498\mathrm{i}$, and the other parameters used are given in Table 5.1.

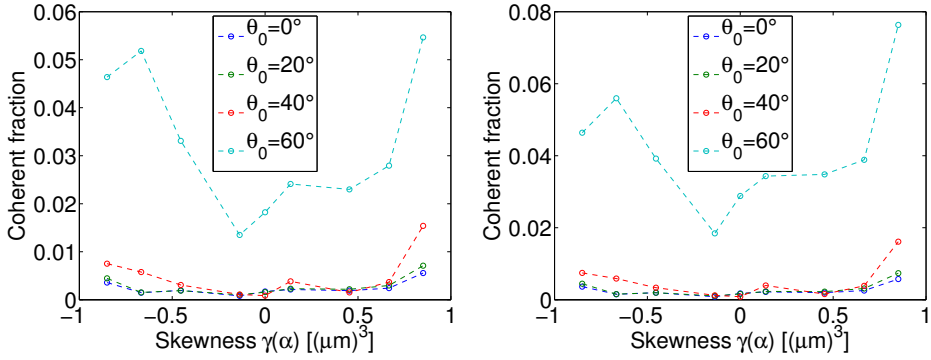

Figure 6.6: Coherent fraction of the scattered intensity from a weakly rough surface for p-polarization (left) and s-polarization (right). The circles represent the data points while the dashed lines are interpolations. The dielectric constant was $\varepsilon(\omega) = -17.2 + 0.498\mathrm{i}$, the RMS roughness was $\delta = 0.2\,\mu\mathrm{m}$ and the other parameters used are given in Table 5.1.

6.2 Transparent materials

For the results in this Section the dielectric constant of fused silica glass with a value of $\varepsilon(\omega) = 2.1247 + 0\mathrm{i}$ was used [14], unless stated otherwise. The effect of the surface height skewness on the MDRC was the same as for opaque materials presented in the previous section, and will not be repeated here. As this is a transparent material, the mean differential transmission coefficient (MTDC) will be discussed instead.

6.2.1 MDTC

Figures 6.7 and 6.8 show the MDTCs for fused silica glass and the parameters shown in Table 5.1. It is immediately apparent that there is virtually no difference between positive (left columns) and negative (right columns) skewnesses, and only the magnitude affects the results.

For normal incidence (top row) the transmitted intensity is slightly shifted towards $\theta_t = 0°$ as the magnitude of the surface height skewness increases. A possible explanation for this is that as the peaks get taller or the pits deeper, the surface outside the peaks and pits flattens, as previously discussed. As coherent light is transmitted through a rough surface, the interface acts as a diffusion lens. The coherence is lost and the intensity is spread to other directions than the incident. A rougher surface gives more diffusion, while a flatter surface gives less. Hence, a strongly skewed surface profile, being flatter outside peaks and pits, gives less diffusion. The diffusion effect is demonstrated by the manner in which the transmitted intensity is centred around $\theta_t = \theta_0$, but spread out. If the interface was flat, the MDTC would have the same profile as the incident wave, and sharply peaked around $\theta_t = \theta_0$.

The diffusion effect reverses as the angle of incidence θ_0 becomes large, while the MDTC peak is shifted slightly towards $\theta_t = 0°$. A possible explanation is again rooted in narrow peaks and pits in an otherwise relatively flat surface. While the peaks and pits are 'small' when viewed from normal incidence, their relative size to the surrounding surface increases as they are viewed more from the side. This corresponds to a larger θ_0. Hence, as θ_0 grows, the surface effectively grows rougher, inducing more diffusion.

The observant reader will perhaps recognize the shape of the MDTCs in Figs. 6.7 and 6.8. Indeed, Fig. 6.9 shows an example of an MDTC that is reasonably well approximated by the skew normal distribution presented in Chapter 3. It may seem that the MDTCs are another way of generating skew normal distributions, and that increasing θ_0 is equivalent to decreasing α!

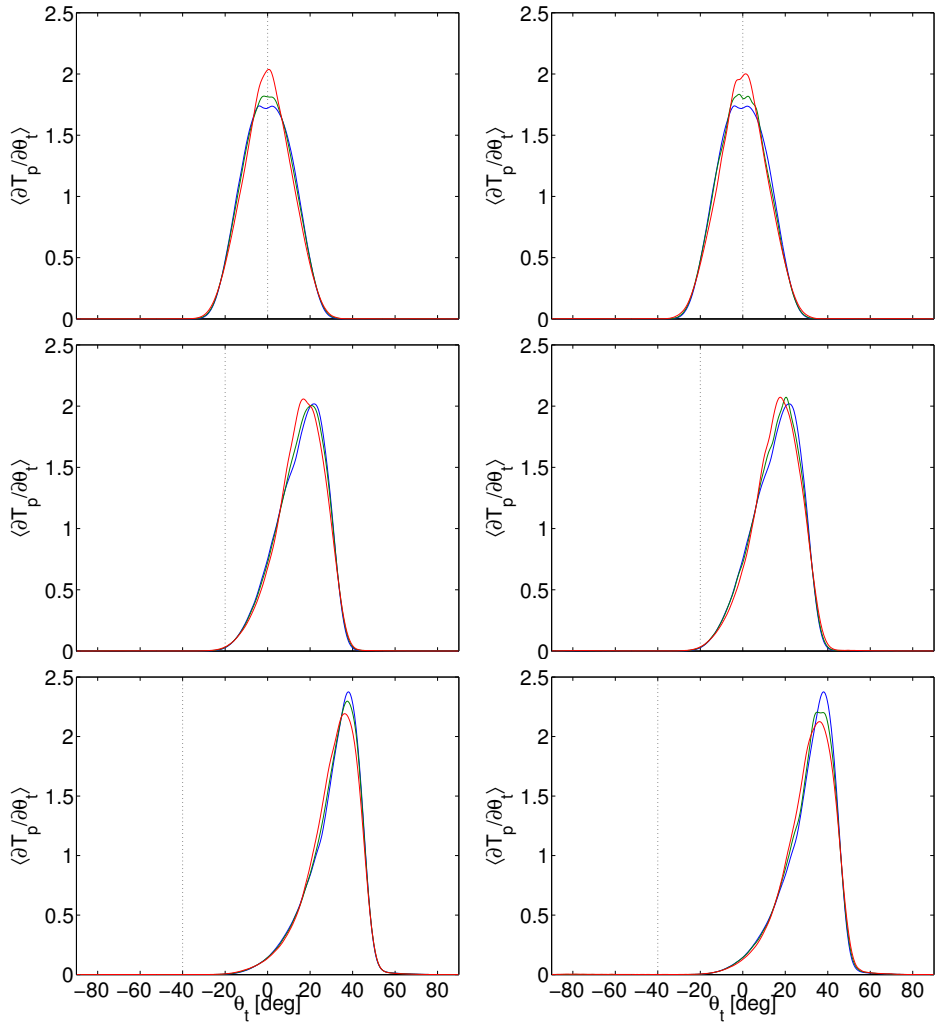

Figure 6.7: MDTC for p-polarization. The left column is for positive skewnesses $\gamma(\alpha)$ with values $\gamma(2) = 0.45\,(\mu\mathrm{m})^3$ (green) and $\gamma(5) = 0.85\,(\mu\mathrm{m})^3$ (red), and the right is for the negative values $\gamma(-2) = -0.45\,(\mu\mathrm{m})^3$ (green) and $\gamma(-5) = -0.85\,(\mu\mathrm{m})^3$ (red). The blue curve is for Gaussian surfaces in both columns. The angles of incidence θ_0 were $0°$, $20°$ and $40°$ for top, middle and bottom row respectively, and are indicated by the vertical dashed lines. The parameters were dielectric constant was $\varepsilon(\omega) = 2.1247 + 0\mathrm{i}$, length $L = 25.6\,\mu\mathrm{m}$, wavelength $\lambda = 0.6127\,\mu\mathrm{m}$ and correlation length $a = 2\,\mu\mathrm{m}$. The other parameters are given in Table 5.1.

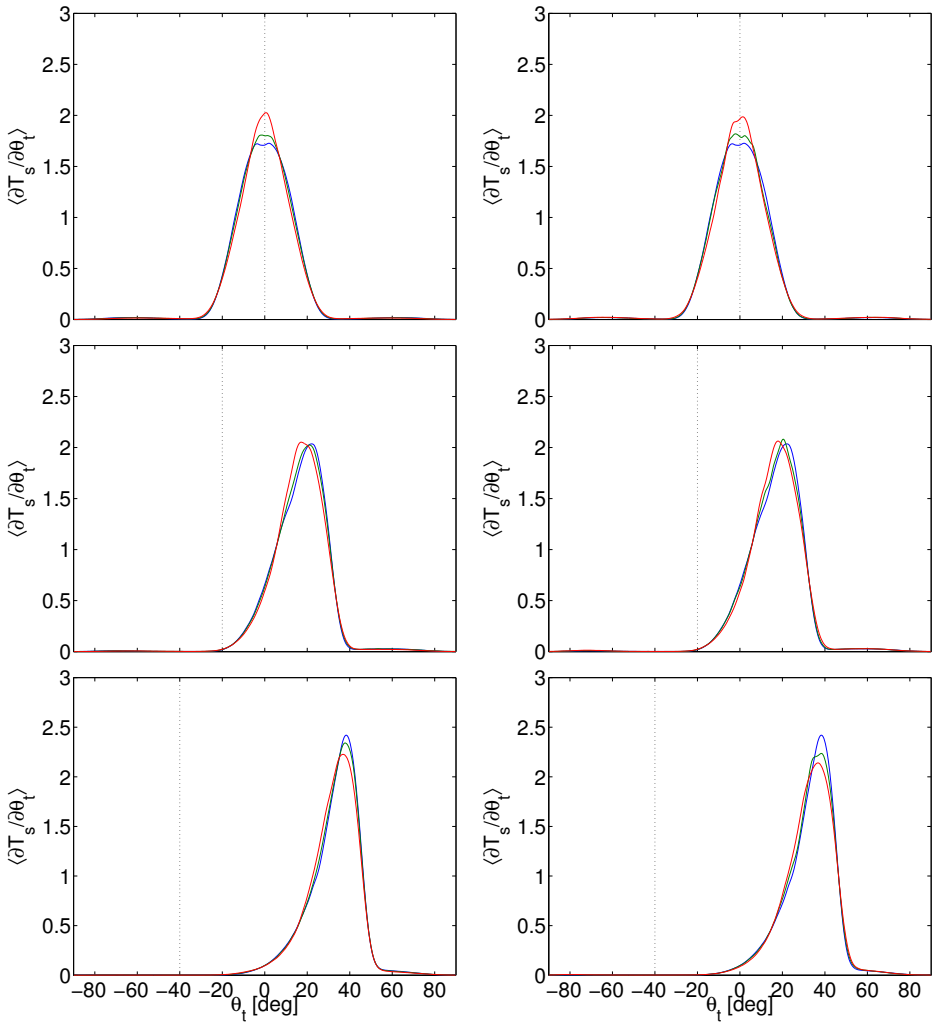

Figure 6.8: Similar to Fig. 6.7, but for s-polarization.

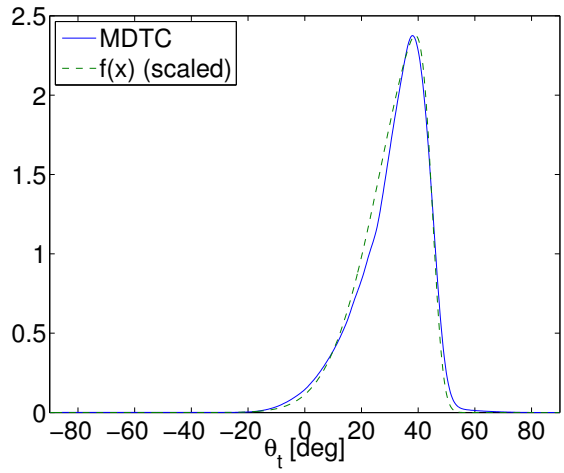

Figure 6.9: MDTC for $\alpha = 0$, $\theta_0 = 40°$ and p-polarization (blue) and $f(x)$ given by Eq. (3.1) (dashed green). The parameters for $f(x)$ are $\xi = 45°$, $\omega = 18°$ and $\alpha = -6$, and a scaling factor of 58. The MDTC is the same as in Fig. 6.7.

6.2.2 Transmittance

The transmittances of the previous MTDCs (as well as for $\theta_0 = 60°$) are shown in Fig. 6.10 for p-polarization (left) and s-polarization (right). The transmittances look fairly constant, indicating that the transmittance is independent of the surface height skewness $\gamma(\alpha)$. One notable exception is found for p-polarization for $\gamma(\alpha) = -0.85\,\mu$m, where the transmittances increase by 1-2% for all θ_0. While it is possible that this is physically real and caused by a scattering phenomenon (for example the effect of Brewster's angle), it is most likely a numerical artefact as seen for the unitarities in Subsection 6.1.2.

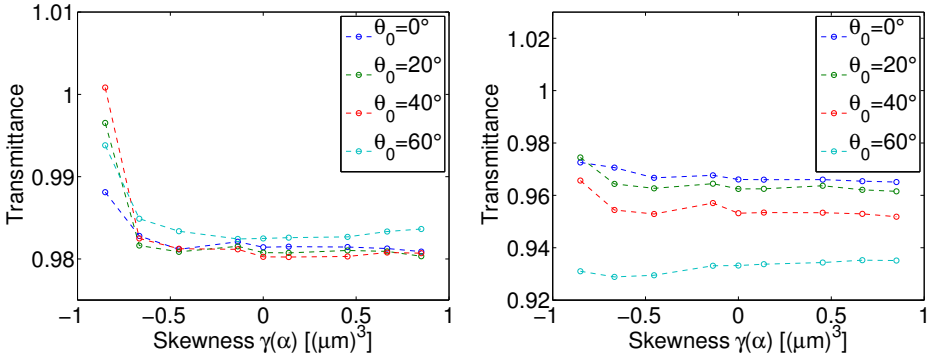

Figure 6.10: Transmittance as a function of surface height skewness for p-polarized (left) and s-polarized (right) light. The dielectric constant was $\varepsilon(\omega) = 2.1247 + 0\mathrm{i}$, and the other parameters used are given in Table 5.1.

Chapter 7

Summary and conclusions

The effect of surface height skewness on rough surface scattering processes has been investigated. To this end, a skewed probability distribution with a corresponding random number generator was needed, as well as a technique for generating rough surfaces numerically.

In Chapter 3, a skew normal distribution was motivated for the chosen skewed probability distribution. A random number generator was implemented in Fortran 90 and verified to give the expected results.

In Chapter 4, a surface generation surface algorithm described by Nichols et al. was implemented in Fortran 90 to generate properly correlated surfaces from the random numbers, and the algorithm was verified to give consistent results. The limitations of the algorithm were outlined, and its advantages and drawbacks were compared to the method of Fourier filtering.

In Chapter 5, the surface generator was integrated into the simulation program Maxwell1D, a program created by I. Simonsen to numerically simulate the scattering of an electromagnetic field incident on a rough interface. The necessity of applying a wavelet filter on the surfaces was justified, after which the generated surfaces proved able to reproduce known results for the case of a Gaussian height distribution.

In Chapter 6, the results for rigorous simulations of scattering from surfaces with different surface height skewnesses are presented and discussed. Both the reflection from non-transparent (opaque) materials and the transmission from transparent materials were examined.

For the reflection from opaque materials, strongly skewed surface heights induced more scattered intensity in the forward directions, both for positive and negative values of the skewness. The proposed explanation is a model for a surface with strongly skewed heights where the surface is relatively flat between sharp

peaks or deep pits. A flatter surface scatters more intensity in the forward directions. For negative values of the skewness, there was an additional increase in the scattered intensity for scattering angles $\theta_s = [60°, 90°]$. This phenomenon was attributed to the lack of peaks to scatter the intensity for these directions. Similarly, the scattered intensity showed a negative correlation with the surface height skewness for oblique angles of incidence for scattering angles $\theta_s = [-60°, -90°]$. Whereas a peak has a relatively large probability of scattering the incident field in these directions, as pit correspondingly has a smaller probability. The results also showed a negative correlation between the surface height skewness and the size of the enhanced backscattering peak. This was attributed to the fact that the multiple scattering events that cause the enhanced backscattering peak to occur, happen more frequently in a pit (negative skewness) than between peaks (positive skewness). There were no strong indications for a correlation between surface height skewness and absorption in absorbing materials, but a strongly skewed surface height profile (both positive and negative skewness) seemed to induce slightly more coherent scattering for weakly rough surfaces. This is again explained by a relatively flat surface between peaks and pits.

For the transmitted field from transparent materials, the effects of positive and negative values of the surface height skewness were the same, and only the magnitude had an effect. For a normal angle of incidence strongly skewed surface heights induced less diffusion, which is consistent with the model of the surfaces becoming effectively less rough as the magnitude of the skewness increases. For oblique angles of incidence the effect is opposite. The suggested explanation was that the effective size of the peaks and pits as viewed from the source of the field increases when the angle of incidence increases. This causes the 'effective roughness' of the surface to increase, yielding more diffusion. The total transmittance seemed to be independent of the surface height skewness.

Chapter 8

Further work

The main focus of this work has been the reflection and transmission from strongly rough interfaces. However, surfaces may also be weakly rough, as was briefly mentioned in Subsection 6.1.3. For such surfaces, enhanced backscattering from multiple scattering events is very weak, but instead enhanced backscattering may be caused by a phenomenon known as surface plasmon polaritons [1, Sec. 3.4]. A study of the effect of the surface height skewness on this process has not yet been conducted, and is a topic for future research.

The correlation length a and RMS roughness δ were mostly kept constant in this work. Changing the parameters could possibly enhance or reduce the effects of a skewed surface height distribution, and a study of this might give greater insight into the details of the scattering process. Also, other height-height correlation functions might impact the effects of the surface height skewness.

Scattering systems with more than one interface can produce a phenomenon called satellite peaks [1, Subsec. 5.2.2]. Here, a film is placed on top of a material, supporting guided waves. Rigorous numerical simulations could also show how this phenomenon is affected by the skewness of the height of the interface.

In this work, the angular distribution of the scattered intensity was only studied in the far field. By studying the distribution of the tangential component of the field along the surface, the impact of the surface height skewness could also be determined for the near field.

For two-dimensional surfaces, polarization transitions between p- and s-polarizations are possible, and the surface height skewness might enhance or reduce this effect. This would require implementing and testing Nichols' (or an equivalent) algorithm for producing rough surfaces with a height distribution different from the Gaussian in two dimension and is a larger task than the previous suggestions.

Naturally, it would be interesting to see if the results from these simulations

are accurate to results from a lab experiment, and if the predicted effects of increased skewness correspond to the actual effects.

Lastly, as Nichols' algorithm allows surfaces of any height distribution, it is up to the imagination of the reader which distribution(s) might be an interesting case for study.

Bibliography

[1] I. Simonsen. Optics of surface disordered systems. *The European Physical Journal Special Topics*, 181(1):1–103, 2010.

[2] E. Lydersen. Generating randomly rough surfaces with a skewed height distribution. Project assignment, 2013.

[3] C.E. Shannon. Communication in the presence of noise. *Proceedings of the IRE*, 37(1):10–21, Jan 1949.

[4] A.A. Maradudin, T. Michel, A.R. McGurn, and E.R. Méndez. Enhanced backscattering of light from a random grating. *Annals of Physics*, 203(2):255 – 307, 1990.

[5] N. Wiener. Generalized harmonic analysis. *Acta Mathematica*, 55(1):117–258, 1930.

[6] A. Azzalini. A class of distributions which includes the normal ones. *Scandinavian Journal of Statistics*, 12(2):pp. 171–178, 1985.

[7] W.H. Press, S.A. Teukolsky, W.T. Vetterling, and B.P. Flannery. *Numerical Recipes 3rd Edition: The Art of Scientific Computing*. Cambridge University Press, New York, NY, USA, 3 edition, 2007.

[8] G. Marsaglia and T.A. Bray. A convenient method for generating normal variables. *SIAM Review*, 6(3):pp. 260–264, 1964.

[9] J.M. Nichols, C.C. Olson, J.V. Michalowicz, and F. Bucholtz. A simple algorithm for generating spectrally colored, non-gaussian signals. *Probabilistic Engineering Mechanics*, 25(3):315–322, 2010.

[10] J.C.S. Santos and M.D. Yacoub. Coloring non-gaussian sequences. *IEEE transactions on signal processing*, 56(12):5817–5822, 2008.

[11] I. Simonsen, Å. Larsen, E. Andreassen, E. Ommundsen, and K. Nord-Varhaug. Haze of surface random systems: An approximate analytic approach. *Phys. Rev. A*, 79:063813, Jun 2009.

[12] E.R. Mendez and K.A. O'Donnell. Observation of depolarization and backscattering enhancement in light scattering from gaussian random surfaces. *Optics Communications*, 61(2):91 – 95, 1987.

[13] E.D. Palik. *Handbook of optical constants of solids*, volume 3. Academic press, 1998.

[14] M. Bass, C. DeCusatis, J. Enoch, V. Lakshminarayanan, G. Li, C. MacDonald, V. Mahajan, and E. Van Stryland. *Handbook of Optics, Third Edition Volume IV: Optical Properties of Materials, Nonlinear Optics, Quantum Optics (set)*. Handbook of Optics. McGraw-Hill Education, 2009.

Appendix A

Variances of higher moments

The variance of the second moment is easily calculated using the properties of the skew normal distribution. Property H in Ref. [6] says that if Z is a skew normal distributed variable with $\xi = 0$ and $\omega = 1$, then Z^2 is χ^2 distributed with one degree of freedom. This gives $\mathrm{Var}(Z^2) = 2$. If X is a skew normal variable with $\mathrm{E}(X) = 0$ and $\mathrm{Var}(X) = 1$, then $(X + \mathrm{E}(Z)) \cdot \sqrt{\mathrm{Var}(Z)} \sim Z$. Using $\mathrm{Var}(aX + b) = a^2 \,\mathrm{Var}(X)$ and $\mathrm{Var}(X) = 1$ gives

$$\begin{aligned} \mathrm{Var}(Z^2) &= \mathrm{Var}\left((X + \mathrm{E}(Z)) \cdot \sqrt{\mathrm{Var}(Z)})^2\right) \\ &= (\mathrm{Var}(Z))^2 \cdot \mathrm{Var}\left(X^2 + 2X\,\mathrm{E}(Z) + (\mathrm{E}(Z))^2\right) \\ &= (\mathrm{Var}(Z))^2 \cdot \left(\mathrm{Var}(X^2) + 4(\mathrm{E}(Z))^2\right) = 2, \end{aligned} \tag{A.1}$$

which gives

$$\mathrm{Var}(X^2) = \frac{2}{(\mathrm{Var}(Z))^2} - 4(\mathrm{E}(Z))^2. \tag{A.2}$$

The expectation and variance of Z are given in Eqs. (3.8) and (3.9) with $\xi = 0$ and $\omega = 1$. The variance of X^2 is α dependent, due to the α dependence of $\mathrm{E}(Z)$ and $\mathrm{Var}(Z)$. Finally, for the average $\langle X^2 \rangle$ of a large sample of N numbers, the second moment has a normal distribution with expectation $\mathrm{E}(X^2) = \sigma$ and standard deviation

$$\sigma(\langle X^2 \rangle) = \sqrt{\frac{\mathrm{Var}(X^2)}{N}} \tag{A.3}$$

according to the central limit theorem.

The variance of the third moment is not as easily calculated. The most obvious method is to use the method of moments and find

$$\mathrm{Var}(X^3) = \mathrm{E}\left((X^3)^2\right) - \left(\mathrm{E}(X^3)\right)^2 .$$

The expectation values can be found using Eq. (3.5), but this quickly turns cumbersome as it involves differentiating Eq. (3.7) six times using the chain rule. However, software allowing algebraic manipulation of expressions such as Maple handles this well, and the code

$$\begin{aligned}
&Mz := t \mapsto \mathrm{e}^{1/2\,\xi\,t+1/2\,\omega^2 t^2}\left(1+\mathrm{erf}\left(1/2\,\delta\,\omega\,t\sqrt{2}\right)\right)\\
&f := t \mapsto \tfrac{d^6}{dt^6}Mz\,(t) - \left(\tfrac{d^3}{dt^3}Mz\,(t)\right)^2\\
&VarGamma := eval\,(f\,(t), t=0)\\
&VarGamma := eval\left(VarGamma, [\xi = -\omega\,\delta\,\sqrt{2\,\pi^{-1}}]\right)\\
&VarGamma := eval\left(VarGamma, [\omega = \left(1-2\,\tfrac{\delta^2}{\pi}\right)^{-1}]\right)\\
&VarGamma := eval\left(VarGamma, [\delta = \tfrac{\alpha}{\sqrt{1+\alpha^2}}]\right)\\
&stdGamma := \sqrt{VarGamma}\\
&simplify\,(stdGamma)
\end{aligned}$$

gives the standard deviation

$$\begin{aligned}
\sigma(X^3) = \pi^{3/2}\frac{\left(1+\alpha^2\right)^3}{2\left(\pi+\pi\,\alpha^2-2\,\alpha^2\right)^6}\,&\left(-18\,\alpha^6-75\,\pi\,\alpha^6-104\,\pi^2\alpha^6\right.\\
&+60\,\pi^3\alpha^6-312\,\pi^2\alpha^4+180\,\pi^3\alpha^4-135\,\pi\,\alpha^4\\
&\left.-288\,\pi^2\alpha^2+180\,\pi^3\alpha^2+60\,\pi^3\right)
\end{aligned} \tag{A.4}$$

for the distribution scaled so that $\mathrm{E}(X) = 0$ and $\mathrm{Var}(X) = 1$. Finally, for the average $\langle X^3\rangle$ of a large sample of N numbers, the third moment has a normal distribution with expectation $\mathrm{E}(X^3) = \gamma$ and standard deviation

$$\sigma(\langle X^3\rangle) = \frac{\sigma(X^3)}{\sqrt{N}} \tag{A.5}$$

according to the central limit theorem.